Chapter 2
Ductile Ceramics

Abstract Not all ceramics are brittle at room temperature. There are some ceramics which are ductile at ambient temperatures. Such ceramics, for example are single crystals MgO, $SrTiO_3$, etc. They undergo plastic deformation and by dislocation motion slip lines are observed on the deformed specimens. In pure MgO at room temperature, dislocations are very mobile at comparatively low stresses. Changing the microstructure, possibly by alloying, the mobility of dislocations may be reduced and an increase in strength may be achieved. As usually observed, material undergoing plastic deformation tend to strain harden, a feature observed also in ductile ceramics. Of the several factors influencing the strength properties of ductile ceramics, grain size is outstanding. Fine grained ceramics are desirable. Originally brittle ceramics show elongation at high temperatures which is a usual observation. There is a transition temperature from brittle to ductile behavior which depends on the ceramics. One of the common methods to determine the brittle to transition temperature is by impact testing, and for this purpose various sophisticated machines have been developed. An extraordinary phenomenon related to ductility is superplasticity, where very high values of strains can be achieved before fracture. Superplastic ceramics are oxide (zirconia) or non-oxide ceramics. Well-known superplastic ceramics are SiC and FeC. The common feature of superplastic materials is the requirement of very fine grains, namely, in the nanosize range.

2.1 Introduction

This chapter considers the mechanical properties of ductile ceramics, which can be grouped into three categories as classified below:

(a) Ductility at elevated temperatures. As is commonly known, some ceramics are ductile at high temperatures and it is meaningful to consider brittle–ductile transition. This was mentioned in Chap. 1, Sect. 1.11 on the Impact Testing of Ceramics.

J. Pelleg, *Mechanical Properties of Ceramics*, Solid Mechanics and Its Applications 213, DOI: 10.1007/978-3-319-04492-7_2,

(b) Ductile ceramics that show plasticity at ambient temperatures. Their features and, in some cases, modifications in their compositions are significant. Furthermore, certain additions to base ceramics, those which promote ductility (such as metals), are considered.
(c) Superplasticity in ceramics. Some ceramics show plastic behavior with elongations of ~ 100 % and more. This is an important feature of this class of ceramics, because it is of structural interest for technical or industrial applications.

2.1.1 Ceramics at Elevated Temperatures

The most outstanding feature of ceramics in this category is the various degrees of plasticity that occur following the transition from brittle to ductile condition. This is the first transition to be discussed here, since all the other features are consequences of the brittle-to-ductile transition (henceforth: BDT).

2.1.1.1 Transition Temperature

The classic method for evaluating the transition temperature from a ductile to a brittle state is by impact testing. The basic reasons for using such a test are the high strain rate that can be achieved by impact and its simplicity. Though there are currently many other ways to vary strain rate, those who choose to perform impact tests can enjoy the use of modern, instrumented impact machines. For most ceramics which are brittle at room temperature (henceforth: RT), ductility is a high-temperature feature; thus, it is more meaningful to discuss BDT, rather than ductile-to-brittle transition (DBT), the more common nomenclature.

Relatively few impact strength data are available in the literature on ceramics and there are even fewer recorded experimental reports. The major limitations of performing such impact tests are the brittleness and low impact strength of ceramics at low and ambient temperatures, especially when the focus is on their applications at elevated temperatures, in light of their high strength properties.

For an early work on the determination of the transition temperature by impact, one may consult the paper by Kingery and Pappis [29]. Above a critical transition temperature, ductility increases markedly and ductile fractures are observed in ceramics. An illustration of the transition temperatures for a few ceramics may be seen in Fig. 2.1.

The experimental set-up for impact loading is shown in Fig. 2.2. The samples are cylindrical, 6 in. long and $^1/_2$ in. in diameter, supported on dense, sintered alumina knife edges across a $4^1/_2$ in. span.

The furnace is heated with silicon carbide resistant elements to 1600 °C. The samples were impacted in the furnace by a pendulum hammer having a 23.65 in. arm length and a 0.411 lbs wedge-shaped, sintered alumina head, as shown in Fig. 2.2.

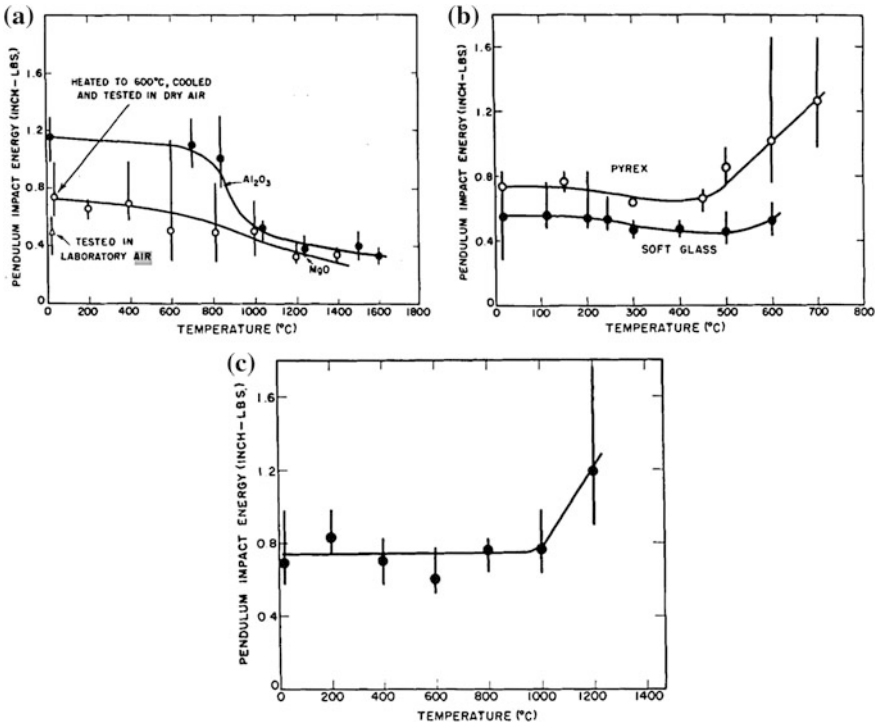

Fig. 2.1 Impact strength of: **a** $A1_2O_3$ and MgO; **b** Pyrex and soft glass; **c** semivitreous whiteware body [29]. With kind permission of Wiley and Sons

Tests were performed until fracture occurred after successive blows of the hammer. About 12 specimens were tested at each temperature. The pendulum velocity at impact was approximately 41 in./s.

These impact test outcomes are different from the familiar impact results for metals, where impact strength increases above the transition temperature; this is not observed in Al_2O_3 and MgO. Furthermore, in all these cases, an examination of the fracture surfaces indicates that brittle fracture has occurred, whereas the fracture in metals is ductile. The transition temperature in Al_2O_3 is about 900 °C. Both the soft glass and Pyrex-brand glass samples showed little variation of impact strength at temperatures up to 500 °C, which can be considered their transition temperatures. However, the results for Pyrex are questionable, because the specimen slumped at $\sim$600 °C. The semivitreous, white-ware body tested showed no variation in impact strength at temperatures up to 1000 °C, its probable transition temperature. The 900 °C temperature, in the case of Al_2O_3, at which the impact strength decreases, is about the temperature at which plastic flow and creep commence. The expectation that, by analogy with metals, an increase in impact strength and ductile failure should also be observed at sufficiently high temperatures for ceramics was not observed in these impact tests.

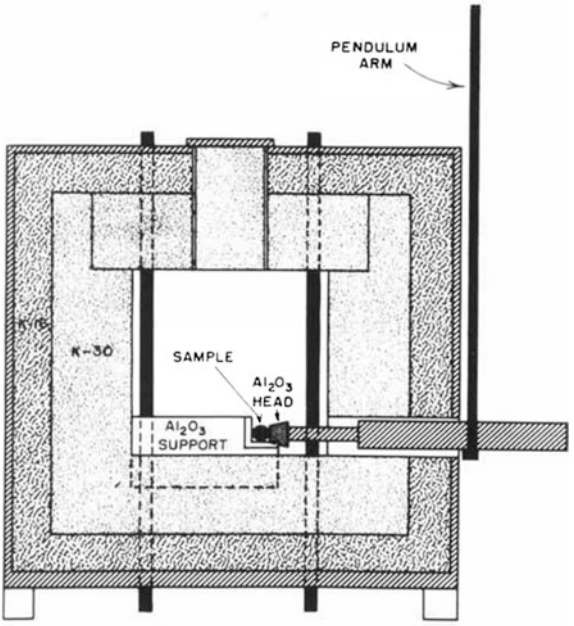

Fig. 2.2 The apparatus for impact testing at elevated temperatures [29]. With kind permission of Wiley and Sons

Recent experiments, however, determine transition temperature by varying the strain rates, whereas, in the impact tests, the information is obtained at the single strain rate characteristic of the given machine. Strain rate influences transition temperature both in single crystals and in polycrystalline materials. Moreover, in single crystals all the effects should be taken into account. In Fig. 2.3, the influence of orientation is indicated. Here, the BDT of precracked sapphire in four-point bending is shown as a function of orientation and strain rate from RT to 1500 °C. As can be seen in the figures below, T_c specimens fracture at the stresses indicated in the temperature range ~20–1000 °C. Above T_c, specimens exhibit general yield with a yield stress that falls with decreasing temperature. Transition occurs at the temperature at which the yield stress in bending is equal to the fracture stress for the specimen geometry used. T_c is the BDT of the specimens shown.

These tests were performed using an Instron Model 8561 (single screw) machine in air and the furnace was adapted to perform four-point bend tests. The rates indicated in Fig. 2.3 relate to crosshead displacement. Figure 2.4 shows the resolved shear stress at yield for the specimens tested at $\dot{e} = 4.2 \times 10^{-7}\ s^{-1}$ above T_c at the indicated orientations. The mechanism for slip is dislocation glide, which explains the orientation dependence of yield, as seen in Fig. 2.4. Thus, the BDT temperature, T_c, of the sapphire (Al_2O_3) varies not only with the strain rate, but also with the crystallographic orientation of the fracture plane.

The activation energy of the process controlling the BDT in sapphires, derived from the strain rate variation of T, is approximately 3.2 eV, close to that for dislocation glide. This was obtained by the Eq. (2.1):

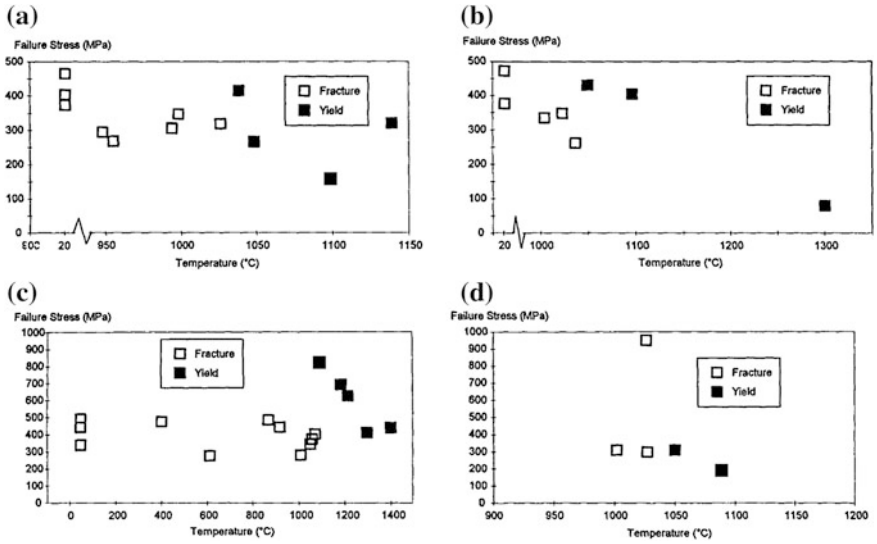

Fig. 2.3 Fracture stress versus temperature data: **a** specimens of orientation **A** (1012) (transition temperature, T = 1035 ± 5 °C), **b** specimens of orientation **B** (1105) (T = 1055 ± 5 °C), **c** specimens of orientation **C** ($11\bar{2}0$) (T = 1090 ± 10 °C), **d** specimens of orientation **D** (0001) (T = 1025 − 1050 °C). $\dot{e}\imath = 4.2 \times 10^{-7} s^{-1}$ for (**a**), (**b**) and (**c**), and 1.3×10^{-6} s^{-1} for (**d**) [26]. With kind permission of Wiley and Sons

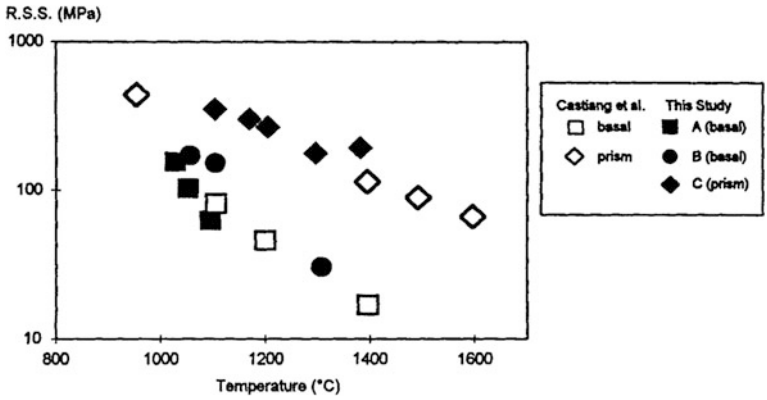

Fig. 2.4 Critical resolved shear stress for yield (above the transition temperature) in bending for all specimens tested at $\dot{e} = 1.3 \times 10^{-6} s^{-1}$ compared with data obtained by compression tests of Castaing et al. **C** specimens show prismatic slip and those of **A** and **B** show basal slip [26]. With kind permission of Wiley and Sons

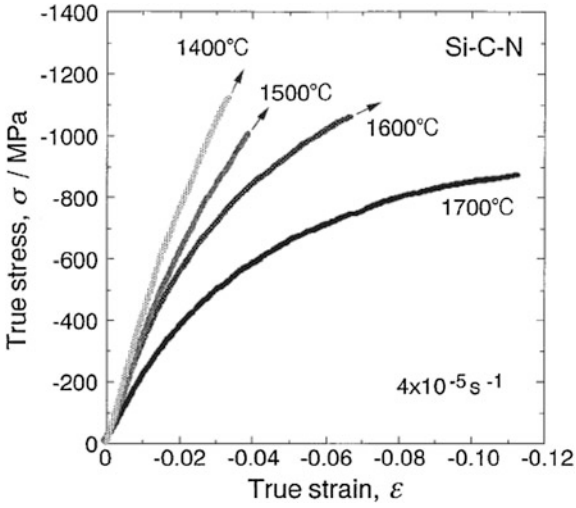

Fig. 2.5 Stress–strain curves of the Si–C–N ceramics tested in compression at high temperatures in the 1400–1700 °C range at a strain rate of 4×10^{-5} s^{-1} [25]. With kind permission of Etsuko Hasebe of the editorial staff of the Japan Institute of Metals (JIM)

$$\dot{e} = \exp\left(-\frac{E_a}{kT}\right) \tag{2.1}$$

The plastic deformation of the sapphire occurred due to basal and prismatic slip during loading above T. Basal slip was found in **A**- and **B**-oriented specimens and prismatic slip in **C**-oriented specimens. The resolved stresses at yield (according to the author) are comparable to those measured by other researchers under compression in the appropriate slip system.

Note that the impact BDT in Al_2O_3, as indicated above, is $\sim$900 °C, whereas for sapphires it was $\sim$1000 °C. The reason for this may be that, in polycrystalline Al_2O_3, grain-boundary sliding contributed to the onset of plastic flow, which is absent in single crystal Al_2O_3. The effect of strain rate on BDT is observed also in superplastic deformation, discussed below in Sect. 2.2c.

2.1.1.2 Ductility and Strength

Not unlike the case of superplastic ceramics, ductility and strength relations are influenced by strain rate. The conditions of the experiment must be above the DBT to observe plastic flow, which is different for various ceramics. An illustration of the effect of strain rate and temperature on the strain (ductility) at some stress level can be seen in monolithic Si–C–N. Silicon–nitride-based ceramics are quite promising candidates for mechanical applications at elevated temperatures. Specimens were prepared by hot isostatic pressure (henceforth: HIP) of pyrolyzed powder compact at 1500 °C and 950 MPa, without any sintering additives. These compression tests were conducted at temperatures from 1400 to 1700 °C in a nitrogen atmosphere with a servo-hydraulic-type testing machine at constant crosshead speed in an induction heating furnace. In Fig. 2.5, stress–strain curves

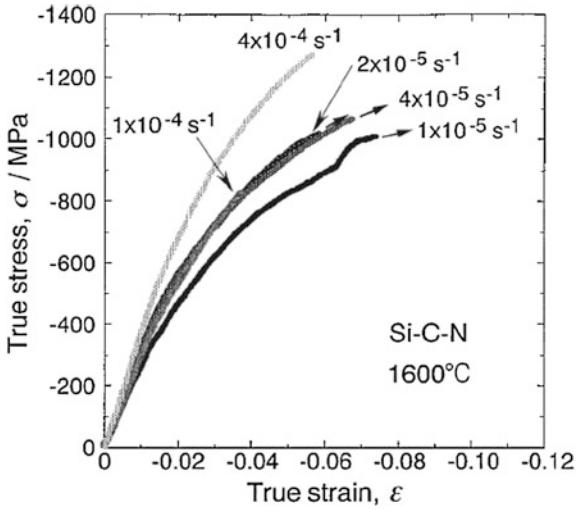

Fig. 2.6 Stress–strain curves of the Si–C–N ceramics tested in compression at 1600 °C at various strain rates [25]. With kind permission of Etsuko Hasebe of the editorial staff of the Japan Institute of Metals (JIM)

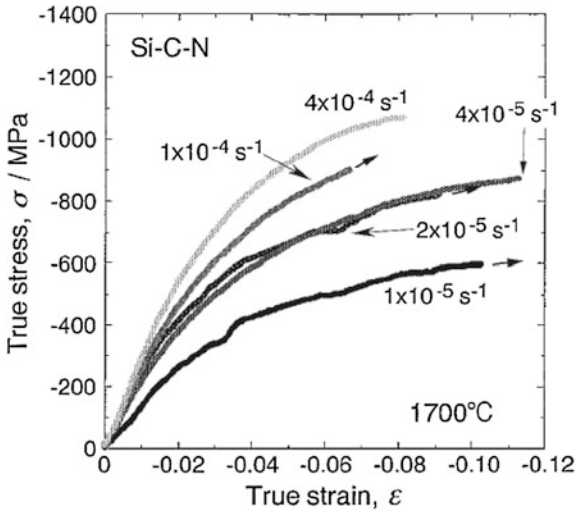

Fig. 2.7 Stress–strain curves of the Si–C–N ceramics tested in compression at 1700 °C at the strain rates indicated [25]. With kind permission of Etsuko Hasebe of the editorial staff of the Japan Institute of Metals (JIM)

obtained by compression tests at various temperatures and at an initial strain rate of 4×10^{-5} s^{-1} are shown.

The arrows in the curves indicate the locations where the tests were interrupted. In curves when no arrows are shown, the specimen has failed at the end of the curve. Deviation from linearity may be seen even at 1400 °C, but at this temperature and at 1500 °C, only slight plastic deformation was observed, in spite of the high compressive stress over 1000 MPa. At the same stress, a compressive strain of $\sim$7 % was obtained at 1600 °C. Yet, a compressive strain of about 11 % was achieved at 1700 °C at a lower compressive stress. Figures 2.6 and 2.7 illustrate compressive stress–strain curves at various strain rates at 1600 and 1700 °C.

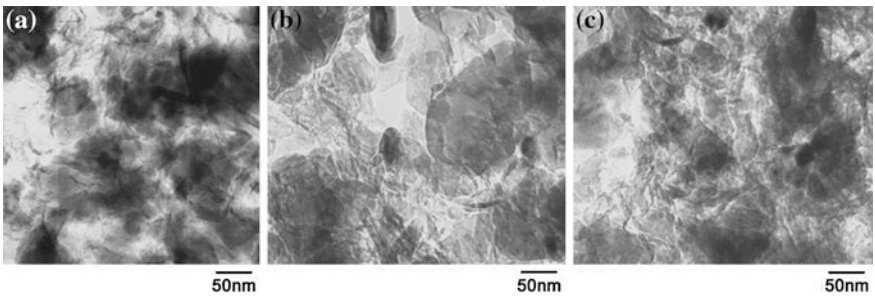

Fig. 2.8 TEM micrographs of the Si–C–N ceramics, **a** before test (as-HIP-treated), and after compression tests at **b** 1700 °C, 2×10^{-5} s^{-1}, and **c** 1700 °C, 4×10^{-5} s^{-1} [25]. With kind permission of Etsuko Hasebe of the editorial staff of the Japan Institute of Metals (JIM)

The strain-rate exponent of the compressive stress in the strain-rate range above 4×10^{-5} s^{-1} at 1600 and 1700 °C is about 0.1. Recall that the strain rate is related to stress as:

$$\sigma = C\dot{\varepsilon}^{m}|_{\varepsilon,T} \tag{2.2}$$

where m is strain-rate sensitivity or the strain-rate exponent and $\dot{\varepsilon}$ is the strain rate. Usually, m can be evaluated from the slope of a plot of log σ versus log $\dot{\varepsilon}$. In metals, m is low, <0.1, at RT, but may increase with T. Ceramics fail in pure compression by the coalescence of axially oriented microcracks. Lankford expresses the compressive stress for low rates of loading (10^{-5}–15^{-1} s^{-1}) as:

$$\sigma_c \propto \dot{\varepsilon}^{1/(1+n)} \tag{2.3}$$

Here, σ_c is the compressive strength, n is the stress-intensity exponent in the macroscopic tensile crack velocity relationship and n is in the range 50–200. Equation (2.3) expresses a relatively strain-rate insensitive process controlled by the thermally-activated growth of microcracks. This process is said to dominate the compressive failure of some ceramics, such as Al_2O_3, SiC and Si_3N_4. An additional equation (Grady and Lipkin) predicts a transition from the dependence expressed by Eq. (2.3) to one given as:

$$\sigma_c \propto \dot{\varepsilon}^{-1/3} \tag{2.4}$$

which occurs at a material-dependent characteristic strain rate that, for most ceramics, lies within the range of 10^3–10^4 s^{-1}.

TEM micrographs of these specimens after the compression tests at 1700 °C are shown in Fig. 2.8, together with the results of the pretest sample.

The microstructure before the test (Fig. 2.8a) is a fine, two-phase structure, consisting of roundish Si_3N_4 crystalline grains, 20–80 nm in size, in a turbostratic, graphite-like phase. These phases are homogeneously distributed. The microstructures of the specimens after the compression tests, at both the initial strain

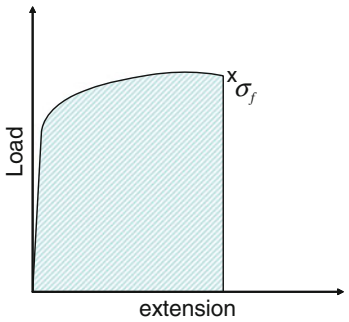

Fig. 2.9 Schematic curve for toughness

rates of 2×10^{-5} s^{-1} (Fig. 2.8b) and 4×10^{-5} s^{-1} (Fig. 2.8c), also consist of Si_3N_4 and graphite-like phases, similar to the structure before the test. However, the Si_3N_4 grains in the structures at both the initial strain rates were considerably coarsened during testing. The sizes of the Si_3N_4 grains after the compression tests were about 200 and 150 nm for the 2×10^{-5} and 4×10^{-5} s^{-1}, respectively.

Si–C–N ceramics maintained their mechanical strength up to 1500 °C and plastic flow was observed during the compressive stress tests at 1600 and 1700 °C, making Si–N-based ceramics one of the most promising candidates for mechanical applications at elevated temperatures.

2.1.1.3 Toughness

In defect-free solid materials, the ability to absorb energy, expressed by the area under the stress–strain curve, is known as 'toughness'. This represents the resistance of a material to fracture and is expressed as the amount of energy per volume having the units $\left[\frac{kg}{m^2} \times \frac{m}{m} = \frac{kg.m}{m^3}\right]$, given in SI system notation as joules per cubic meter (J/m^3). For such defect-free solids (as in the case of metals), the relation is:

$$U_T = area\ under\ the\ curve = \int_0^{e_f} \sigma\, de \tag{2.5}$$

Graphically, the area under the curve and up to the fracture is shown in Fig. 2.9.

In Eq. (2.5), the elastic contribution is neglected. Toughness and strength are related, but not necessarily the same, especially when brittle and ductile materials are considered. Whereas strength indicates how much force a material can support before breaking, toughness shows how much energy a material can absorb before fracture. A material may be strong and tough, if it fractures by withstanding a high force and exhibits high strain, but brittle materials with high strength (∼equal to its yield stress) may be strong, but not tough, since their strain values are limited. Variables that greatly influence the toughness of a material are: strain rate (rate of loading), temperature and notch effect (for more details see [7]).

The fracture toughness [7] resulting from crack propagation is related to a critical stress intensity factor, K_c, which is a measure of fracture toughness representing the resistance of the material to failure from fracture initiated by a preexisting crack. One may add to the aforementioned variables that influence toughness: loading rate, composition, environment, microstructure and the tip geometry. A subscript is used to denote the crack opening mode to K_c and the equation can be expressed as:

$$K_{Ic} = \sigma\sqrt{\pi a B} \tag{2.6}$$

Here, a is the crack length and B is a dimensionless parameter. From Eq. (2.6), the critical stress, σ_f, is:

$$\sigma_f = \frac{K_{Ic}}{\sqrt{\pi a B}} = \frac{K_{Ic}}{\alpha\sqrt{\pi a}} \tag{2.6a}$$

and $\alpha = B^{1/2}$. B is a crack length and component geometry factor that is different for each specimen and is a dimensionless parameter. Expressions for α are tabulated for a wide variety of specimen and crack geometries, and specialty finite-element methods are available to compute it for new situations. K_{Ic} values are also used to calculate the critical-stress value, when a crack of a given length is found in a component. The critical-crack length is given from Eq. (2.6) as:

$$a_c = \frac{1}{\pi}\left(\frac{K_{Ic}}{\sigma B}\right)^2 \tag{2.6b}$$

For edge crack, a is the crack length or one-half crack length for internal cracks. In the literature, the above relations are often given in terms of Y, rather than B, with the same meaning. One immediately realizes the connection between this equation and the one derived by Griffith in his theory on brittle fracture.

The best quality ceramics contain imperfections, all of which have remarkable, but detrimental influences on the mechanical properties. Therefore, toughness or rather 'fracture toughness' is of critical importance for design purposes. Like impact tests, a very common method for testing toughness in ceramics is by the introduction of a notch, usually a V notch. Ceramics and ceramic-based composites, having high strength but low crack resistance, are considered for application due to their high strength. However, wide-scale application is still hindered by the presence of cracks. One of the accepted testing methods for the evaluation of critical stress intensity factor, K_{Ic}, is the single-edge, V-notched beam (henceforth: SEVNB) method. Several ceramics (of zirconia, alumina and silicon–nitride ceramics, zirconia and alumina single crystals, silicon carbide, etc.) were tested for fracture toughness by the SEVNB method [17]. V-notched specimens were tested using flexural tests and K_{Ic} values were calculated by means of three-point and four-point flexure tests. The load–deflection diagrams for V-notched specimens contributed to better understanding of the deformation behavior of ceramics at RT and 1300–1400 °C. Figure 2.10 illustrates the effect of V-notch

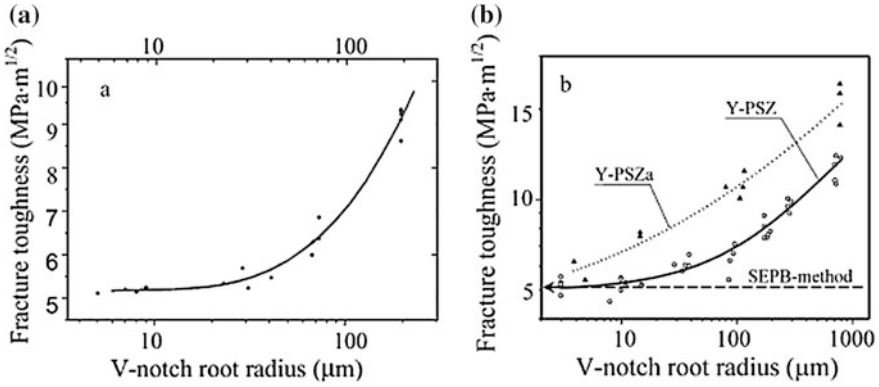

Fig. 2.10 Effect of V-notch root radii on the K_{Ic} values: **a** for Si_3N_4, and **b** for Y-PSZ ceramics [17]. With kind permission of Elsevier

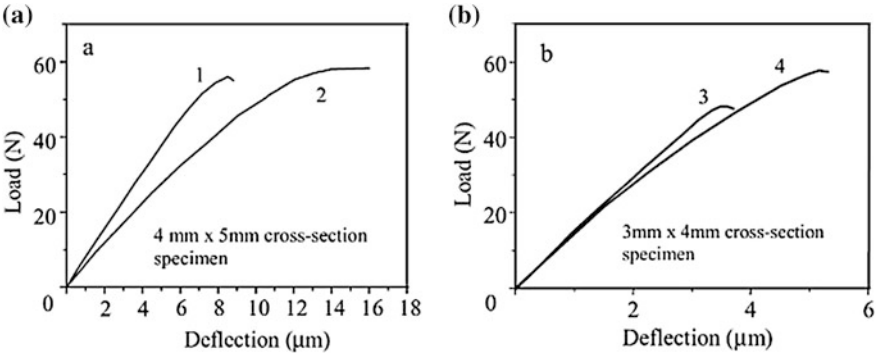

Fig. 2.11 Load-deflection of notched test: **a** Si_3N_4 + 30 % SiC + 3 % MgO; **b** SiC + 50 % ZrB_2 + 10 % B_4C. Specimens 1 and 3 tested at room temperature and specimens 2 and 4 tested at 1400 °C [17]. With kind permission of Elsevier

radii on K_{Ic} values for Si_3N_4 and yttria partially-stabilized zirconia (henceforth: Y-PSZ) ceramics, while the load–deflection relation is illustrated in Fig. 2.11.

Analysis of the data of the fractured specimens reveals that a fracture crack propagated from the points where additional stress concentrations were present. This confirms the assumption that the fracture of a loaded ceramic specimen starts from a small crack ahead of a machined notch root. It is believed that K_{Ic} is influenced more by the sharpness of the notch root, rather than by its shape. The data in Table 2.1 are from three to four-point flexure tests performed on several monolithic ceramics. Table 2.2 shows the K_{Ic} values at RT and high temperatures attained by the SEVNB method for these notched specimens.

Single crystals of zirconia and alumina were tested by SEVNB and by the single-edge notched beam (henceforth: SENB) method, and the results are shown

Table 2.1 Comparative fracture toughness tests (MPa $m^{1/2}$) of several ceramics [17] (with kind permission of Elsevier)

Test method	Three-point flexure (a/W ≈ 0.5)	Four-point flexure (a/W ≈ 0.2. . .0.3)	
		Our results	RRFT'97 results
Si_3N_4	5.5 ± 0.07(5)[a]	5.35 ± 0.16(5)	–
GPSSN	5.3 ± 0.04(5)	5.2 ± 0.18(5)	5.36 ± 0.34(129)
Si_3N_4 + 30 % SiC + 3 % MgO	2.27 ± 0.14(4)	2.40 ± 0.16(5)	–
SSiC	2.45(1)	2.66 ± 0.20(4)	2.61 ± 0.18(56)
SiC + 50 % ZrB_2 + 10 % B_4C	3.59 ± 0.12(3)	3.51 ± 0.15(3)	–
Al_2O_3-998	3.5 ± 0.05(5)	3.6 ± 0.06(5)	3.57 ± 0.22(135)
Y-PSZ	5.7 ± 0.17(5)	5.9 ± 0.19(5)	–

±Standard deviation

[a] The number of specimen tested (in parentheses)

Table 2.2 High temperature fracture toughness test results (SEVNB method) [17] (with kind permission of Elsevier)

Materials	K_{Ic} (MPa $m^{1/2}$)		
	20 °C	1300 °C	1400 °C
Si_3N_4	5.5 ± 0.1	4.2 ± 0.3	–
Si_3N_4 + 30 % SiC + 3 % MgO	2.27 ± 0.1	–	2.68 ± 0.1
SiC + 50 % ZrB_2 + 10 % B_4C	3.52 ± 0.1	3.63 ± 0.3	3.70 ± 0.1
Si_3N_4 [22][a]	5.6 ± 0.5	5.0 ± 0.4	–

[a] The notches were produced by diamond saw with V-shaped tip

Table 2.3 K_{Ic} values for single crystals obtained by SEVNB and SENB methods (MPa $m^{1/2}$) [17] (with kind permission of Elsevier)

Single crystals	Peculiarity	Elastic modulus (GPa)	Test method		Brittleness measure, χ	Index φ
			SENB	SEVNB		
Zirconia	Partially stabilized (3 % Y_2O_3)	245	9.33 ± 0.95	10.33 ± 2.17	1	0.9
Alumina	Specimen axis 45° to optical axis of crystal	403	2.31 ± 0.34	2.45 ± 0.29	1	0.94
	Specimen axis 90° to optical axis of crystal	410	3.19 ± 0.53	2.85 ± 0.50	1	1.12

in Table 2.3. In Table 2.3, χ is a measure of brittleness and is defined by the ratio of the specific elastic energy accumulated in the ceramics by the moment of fracture to the total energy spent on its deformation. χ was evaluated from stress–strain curves obtained during a four-point bend test.

The index of sensitivity, φ, to stress concentrations, which is equal to the ratio of the K_{Ic} values, obtained by the SEVNB and SENB methods is shown in Table 2.3. In the tests of elastic materials, φ ($\chi = 1$) is about 0.6, and in those of inelastic materials, ($\varphi < 1$), exceeding 0.9. Almost all the studies on the deformation behavior of V-notched ceramic specimens with a φ value of about 0.6 produced linear load–deflection diagrams or diagrams with small nonlinearity, as seen in Fig. 2.11 of lines 1 and 3, which are the results of comparatively slow crack growth.

A practical and relatively easy method for obtaining mechanical properties is by indentation tests. For ceramics, the most common methods of performing such tests are the Vickers and the Knoop hardness tests, which are very attractive, practical and relatively less expensive than the other tests discussed in Chap. 1. Assessing the toughness of ceramic materials by means of indentation testing is often done, also due to the ease of performance and low cost of conducting the measurements. Vickers hardness can be expressed [7] as:

$$DPH = HV = 1.854\frac{P}{d^2} = \alpha\frac{P}{d^2} \tag{2.7}$$

P is the load and d is the diagonal. α is a numerical factor (1.854) that depends on shape and it is quoted as ~ 2 for ceramics, as a consequence of using the projected area of the indenter contact with the surface plane. Vickers or Knoop indentations introduce cracks into the ceramics the sizes of which may be measured. The sizes of these artificial surface cracks are related to K_{Ic}. In particular, the lengths of these impression cracks are related to K_{Ic} and the connection between them has been evaluated, for example, by Anstis et al. [11]. A Vickers indentation is performed on a flat ceramic surface so that cracks develop around the indentation. By measuring the crack lengths, it is possible to estimate K_{Ic}, which are in inverse proportion to the toughness of the material. The crack-length method for evaluating toughness, according to Anstis et al. [11] is given by:

$$K_{Ic} = 0.016\left(\frac{E}{H}\right)^{1/2} \times \frac{P}{c^{3/2}} \tag{2.8}$$

Thus, toughness, measured and expressed by K_{Ic}, is dependent on the elastic modulus, E, of the material, its hardness, H, (microindentation is often preferable for the proper evaluation of the indentation crack), crack length, c, and the applied load. Anstis et al. [11] employed a two-dimensional fracture mechanics analysis. The crack length, c, is measured from the center of the impression to the crack tip in meters; E is in GPa and H is the Vickers hardness in GPa. The height of the opposite triangular faces is h. It is clear that under small indentation loads, only small cracks form, as indicated schematically in Fig. 2.12. Actual Vickers indentation cracks are shown in Fig. 2.13. Equation (2.8) is often also expressed as:

$$K_{Ic} = \alpha\left(\frac{E}{H}\right)^{1/2} \times \frac{a^2}{c^{3/2}} \tag{2.8a}$$

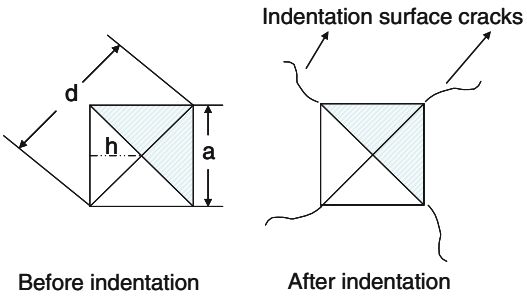

Fig. 2.12 Schematic indentation of a Vickers test before and after indentation. Crack resulting from the indentation are shown

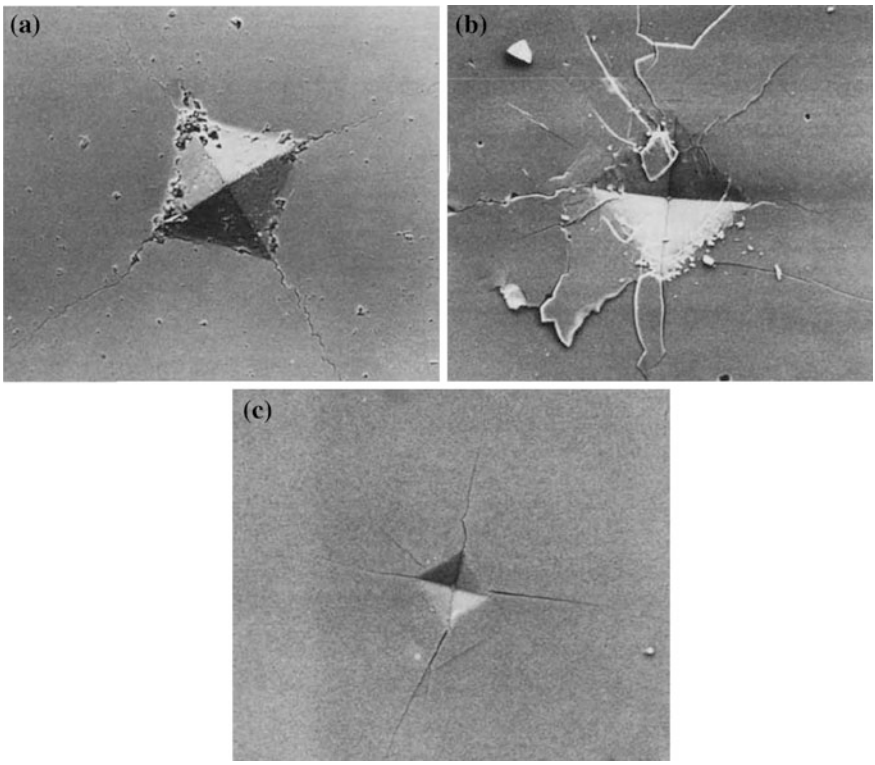

Fig. 2.13 Scanning electron micrographs of radial crack systems of Al_2O_3 in 3 modifications **a** AD999 (P = 50 N), **b** Vi (P = 50 N), and **c** sapphire (P = 10 N), showing the effect of increasing grain size on pattern definition; width of field 200 μm [11]. With kind permission of John Wiley and Sons

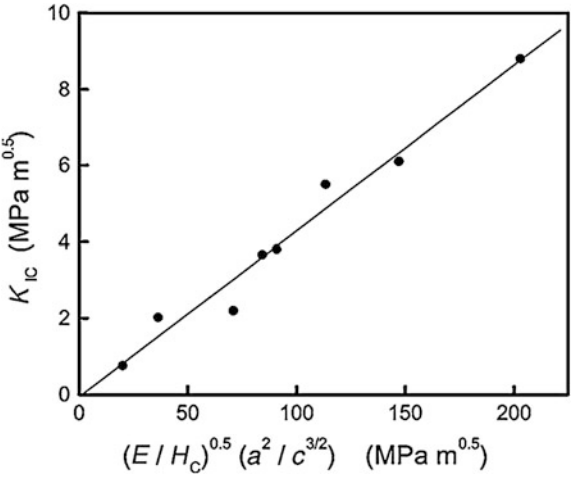

Fig. 2.14 Plot of K_{IC} determined with conventional methods versus the quantity $(E/H_C)^{0.5}(a^2/c^{3/2})$ [19]. With kind permission of Springer

since Vickers hardness may be given in terms of the half-diagonal, a, as:

$$H = \frac{P}{2a^2} \tag{2.7a}$$

by substituting the value of P from Eq. (2.7a) into Eq. (2.8), one obtains Eq. (2.8a).

Equation (2.8a) is expressed in Fig. 2.14 in terms of K_{Ic} versus $\left(\frac{E}{H_c}\right)^{12}\left(\frac{a^2}{c^{3/2}}\right)$.

More about toughness and fracture toughness, expressed in terms of K_{Ic}, will be discussed in the chapter on Fracture in Ceramics.

2.1.1.4 Grain Size Effect

Various strength properties of materials (especially metals) are related to the grain size effect. The well-known, empirical Hall–Petch (henceforth: H–P) relation addresses the grain size effect of these properties [7], expressed as:

$$\sigma_y = \sigma_0 + \frac{k_y}{\sqrt{d}} \tag{2.9}$$

σ_y is the yield stress, σ_0 represents resistance to dislocation glide, k_y is a measure of dislocation pile-up behind an obstacle (a grain boundary, for example) and d is the size of the grain. One may ask how this relates to ceramics. Indeed, various mechanical tests have indicated that the H–P relation also applies to ceramics in many cases [10, 9] and, thus, this relation has been successfully extended to the study of ceramics, as well. Various mechanical properties have been applied to test this relation, but a very common property, hardness, is very often used to indicate the H–P concept. Figure 2.15 shows H–P variation with the grain size of

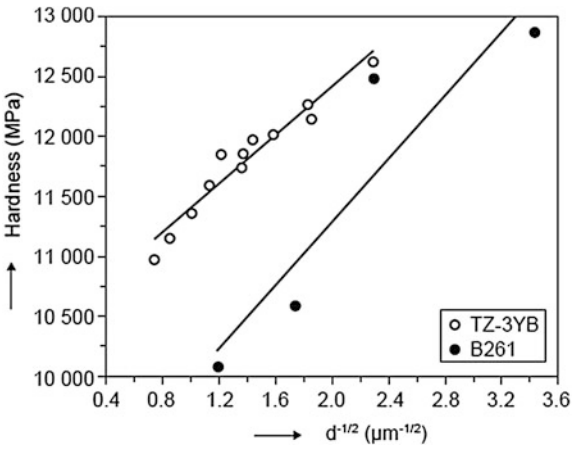

Fig. 2.15 The dependence of the hardness of TZ-3YB and B261 ceramics on the inverse square root of grain size [10]. With kind permission of Dr. Trunec

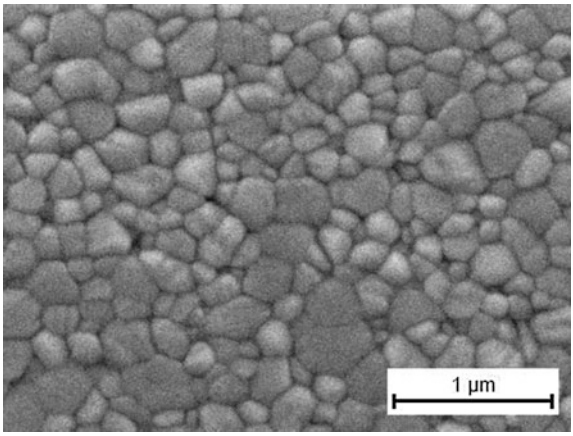

Fig. 2.16 SEM micrograph showing the microstructure of the TZ-3YB ceramics sintered at 1400 °C for 2 h [10]. With kind permission of Dr. Trunec

yttria-stabilized tetragonal zirconia polycrystals (TZ-3YB) and zirconia nano-powder (B261).

The hardness of TZ-3YB ceramics clearly decreases with increasing grain size from HV = 12620 MPa at a grain size of 0.19 μm to HV = 10971 MPa at a grain size of 1.79 μm. The hardness of B261 ceramics shows a higher dispersion, but the linear fit seems to be quite reasonable. These hardness values were determined by Eq. (2.7). The values in the graph may be reasonably expressed by a line ($r^2 = 0.94$), which means that this dependence follows the H–P relation. Figure 2.16 illustrates the microstructure of TZ-3YB.

Miyoshi [36] has confirmed the H–P relation by measuring Wickers hardness as a function of $d^{-1/2}$ for almost the entire grain-size range investigated. Furthermore, using bending strength tests, Rothman et al. [9] reported the adherence to the H–P relation even for spinel, such as magnesium aluminate ($MgAl_2O_4$) (Fig. 2.17).

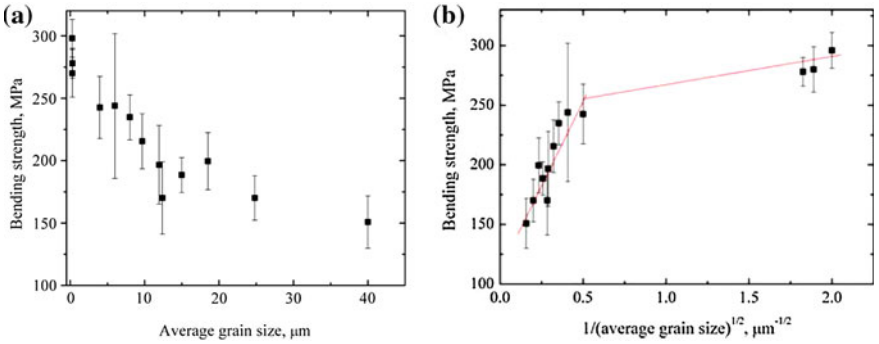

Fig. 2.17 **a** Bending strength as a function of average grain size; **b** shows agreement between the experimental data and the Hall–Petch relation [9]. With kind permission of Mr. Rothman for the authors

The grain-size dependence of mechanical properties is also observed in ceramics. Thus, one can state that the H–P relation is a general observation of most materials, metals and ceramics alike. Deviations from the linear H–P plots, known as the inverse H–P trend, observed in metals having small dimensions, will be discussed later on in the chapter dedicated to that topic.

2.1.1.5 Addition of a Second Phase

A second phase may be either in solution in the matrix or in a state of dispersion. Often, a soluble second phase is in an undissolved stage, since the processing, mainly the thermal treatment, occurs at a low temperature or for an insufficient amount of time for the induction of complete solubility. A second phase may be another ceramic, polymer or metal in various shapes and sizes. Fibers and whiskers are also often used for strengthening ceramic base materials. Here, the focus is on the mechanical properties and not on the influence of a second phase on other physical characteristics (e.g., electrical, magnetic or optical). Furthermore, the method of fabrication of ceramics necessary to densify compacted powder samples (green bodies) in order to form a continuous three-dimensional (henceforth = 3D) structure and, thus, to get ceramic pieces appropriate for the selected application is of critical importance. Moreover the second phase may be crystalline or in an amorphous stage. Although the present objective of adding a second phase is to enhance the mechanical performance of ceramics, it often occurs that the addition of a second phase weakens some mechanical properties, probably due for its promotion of pore formation. An insoluble second phase is a discontinuity in the matrix and, from this standpoint, pores and cracks, though they are not a genuine second phase, may be considered as such.

Usually, the consolidation of the constituents of a ceramic is done by means of a sintering process, which is a densification of the granular (or powder) compact

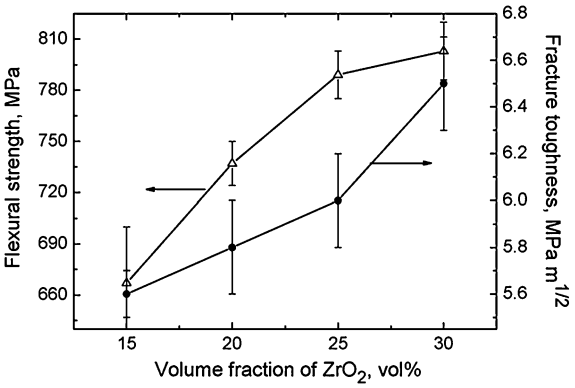

Fig. 2.18 Plots of flexural strength and fracture toughness (by SENB) of hot pressed ZrB_2–ZrO_2 ceramics [34]. With kind permission of Elsevier

by heat treatment. During this stage, the microstructures of the samples evolve into the initial stage of basic ceramics. Note that for maximum densification, HIP is a common practice.

Several examples will be presented to show the influence of a second phase, for example in the ZrB_2 case. There is a growing interest in ZrB_2-based ceramics for their outstanding properties: high melting point, high electrical and thermal conductivities, chemical inertness and good oxidation resistance. These properties make them attractive candidates for high-temperature applications, in which corrosion-wear-oxidation resistance is of interest, for example, for use as ballistic armor, coatings on cutting tools, electrical devices, nozzles etc [16]. Furthermore, refractory diborides exhibit partial or complete solid solution with other transition-metal diborides, which allows compositional tailoring of properties such as the thermal expansion coefficient and hardness.

The fracture toughness of ZrB_2, with and without additives, is generally in the range of 3.5–4.5 MPa $m^{1/2}$. For most applications, however, the value of toughness is unsatisfactory, which hinders its wider use and, therefore, the incorporation of various additives is expected to remedy this problem. ZrO_2 additive was found to improve the mechanical properties of ZrB_2 and to enhance its toughness. Figure 2.18 is an illustration of the effect of ZrO_2 additive in ZrB_2 on flexural strength and fracture toughness.

The densification of ZrB_2–ZrO_2 is improved with increasing amounts of ZrO_2, which is attributed to the smaller grain size of ZrO_2. Denser aggregates are expected to provide better mechanical properties, as indeed observed in Fig. 2.18. Figure 2.19b illustrates the effect of increasing the volume fraction of ZrO_2. Note that the increase of the relative density follows the trend of the plots shown in Fig. 2.18.

Considering the microstructure, energy dispersive spectroscopy (henceforth EDS) patterns reveal that it is characterized by the presence of a coarser and elongated ZrB_2 matrix and relatively finer and equiaxed ZrO_2 grains. This appears in Fig. 2.20. With the increase in the amount of ZrO_2, a denser microstructure is obtained. The fracture surface indicates that ZrB_2 grains fracture predominantly

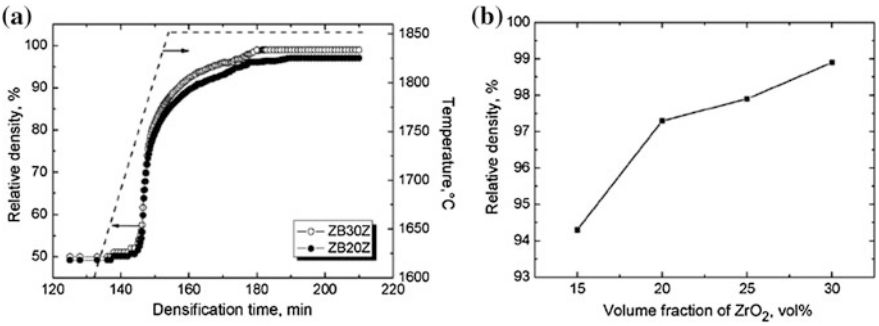

Fig. 2.19 **a** Densification curves of hot-pressed ZB20Z and ZB30Z; **b** relative density (%) of hot-pressed ceramics with increased ZrO_2 content from 15 to 30 vol% [34]. With kind permission of Elsevier

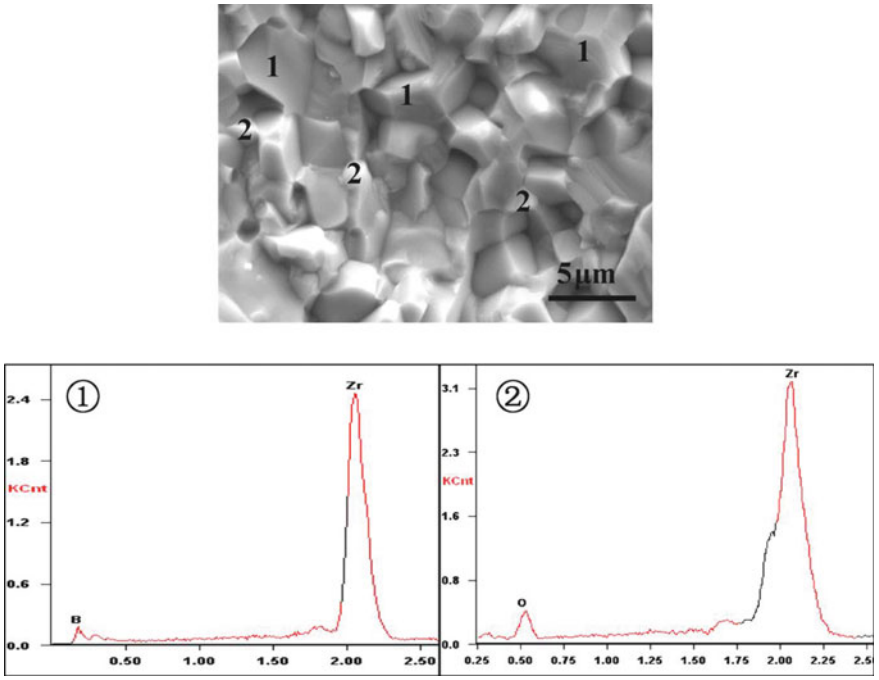

Fig. 2.20 Fracture surface of ZB20Z (ZrB_2-20 vol% ZrO_2), EDS patterns show that the bigger and coarser grains are ZrB_2, the finer and equiaxed grains are ZrO_2 [34]. With kind permission of Elsevier

transgranularly and ZrO_2 grains, which are dispersed among ZrB_2 grain boundaries, fracture intergranularly. The introduction of the smaller second phase of ZrO_2 effectively restrained the growth of grains during hot pressing, becoming more significant with the higher content of ZrO_2.

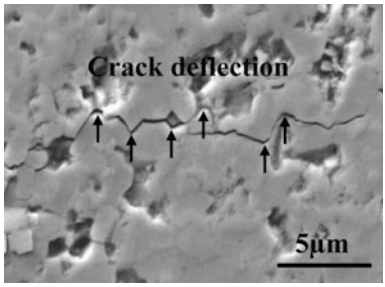

Fig. 2.21 SEM image of microcrack from Vickers indentation on the polished surface of ZB25Z [34]. With kind permission of Elsevier

Flexural strength improved with the increase in the amount of ZrO_2 and the strength increased from 667 MPa for the ZB15Z (ZrB_2-15 vol% ZrO_2) to 803 MPa for the ZB30Z (ZrB_2-30 vol% ZrO_2) ceramics, as indicated in Fig. 2.18. The finer grains are responsible for the improved strength, which can be associated with the H–P relation. Similarly, the increased ZrO_2 content plays an active role in the toughness of the ZrB_2-based ceramics. An increase from 15 to 30 vol% ZrO_2 increases toughness from 5.6 to 6.5 MPa $m^{1/2}$. There are two reasons for this increased toughness: deflection of the crack and stress-induced phase transformation. In the case of crack-deflection toughening, ZrO_2 grains hinder crack growth or its propagation, as indicated in Fig. 2.21. The increase in toughness due to phase transformation is associated with the transformation of tetragonal ZrO_2 into the monoclinic phase. The more tetragonal ZrO_2 is present in the ceramic, the more monoclinic ZrO_2 transformation will occur during the process. Both kinds of toughening, namely, from phase transformation and crack deflection, were largest in ZB30Z (ZrB_2-30 vol% ZrO_2). It is common to express toughness in terms of hardness measurements, involving the dimension of the crack formed on the surface in the vicinity of the indentation, as follows:

$$K_{Ic} = \eta \left(\frac{E}{H}\right)^{2/5} \frac{P}{(al^{1/2})} \tag{2.10}$$

In Eq. (2.10), η is a dimensionless constant for a given indenter geometry, provided the volume is conserved within the 'plastic zone' (adjacent to the indentation). E is the elastic modulus; H is the Vickers hardness; P is the indent load; 2a is the average indentation diagonal length; 2c is the crack length; and $l = c - a$. This relation is applied for toughness where the samples exhibit Palmqvist-type cracks ($0.25 < l/a < 2.5$). The hardness of the ceramic also increases with increasing ZrO_2 and can reach a value of 22.7 GPa under a load of 9.8 N having the composition of ZrB_2-30 vol% ZrO_2. The load dependence of hardness is quite pronounced and the nature of decrease in hardness with increased load has the same form in all ceramics.

A second phase might weaken the ceramics by reducing some of the mechanical properties, probably because, in some way, it promotes pore formation. Above, pores were described as a "discontinuity in the material" and, thus, as having an undesirable effect. In the following, the effect of ceria on the mechanical

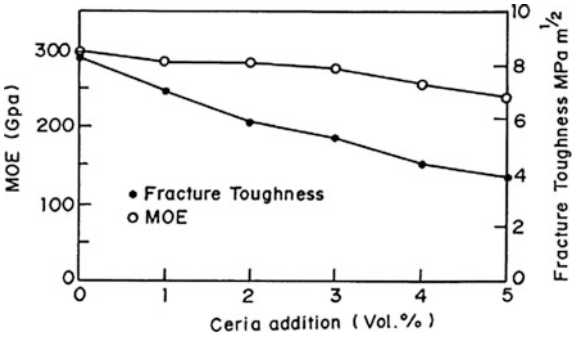

Fig. 2.22 Effect of ceria addition on fracture toughness and modulus of elasticity of ZTA (zirconia toughened alumina) [35]. With kind permission of Elsevier

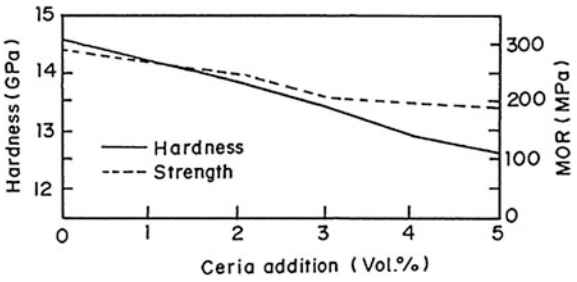

Fig. 2.23 Effect of ceria on hardness and strength of ZTA [35]. With kind permission of Elsevier

properties of yttria-stabilized zirconia-toughened alumina (henceforth: ZTA) will be considered to show how pores can, indeed, degrade mechanical properties. Figures 2.22 and 2.23 clearly show the degradation of the modulus of elasticity (henceforth: MOE), the fracture toughness, the hardness and the modulus of rupture (henceforth: MOR) with the addition of ceria, respectively.

The authors (Mangalaraja et al. [35]) claim that the possible reason for this reduction in strength is due to the high density of the microcracks. As the distances between the microcracks decrease, they near each other and coalescence occurs spontaneously, which substantially reduces the strength of the materials. Moreover, the decreased mechanical properties are found to be due to the higher apparent porosity, possibly resulting from the addition of ceria. The higher degree of apparent porosity is a result of the solid-state mixing of powders.

It was observed that the addition of ceria deteriorates the mechanical properties, including the fracture toughness of yttria-stabilized ZTA, although reports exist to the contrary [46] for polycrystalline yttria-stabilized ZTA, in which fracture toughness is increased by the addition of ceria.

2.1.1.6 Particle Size Effect

The mechanical properties of ceramics are influenced by the particle size of both the base ceramic and of the added phases. Thus, to obtain a fine-grained

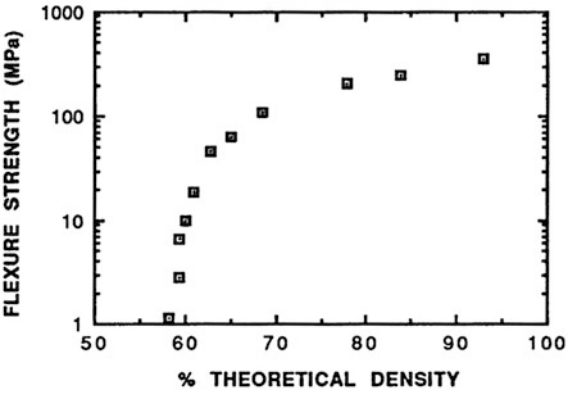

Fig. 2.24 Variation of flexural strength of alumina measured at room temperature after sintering to various temperatures (800–1600 °C). The increase in strength occurs at low theoretical density after which a leveling in strength occurs [5]. With kind permission of John Wiley and Sons

(henceforth: FG), uniform ceramic microstructure after sintering, the distribution of the particle sizes in the slurries of the components (while in the green stage) is of major importance for the production of a high viscosity substance. A proper particle-size distribution facilitates particle arrangement and the development of a relatively dense structural packing. Particle size affects densification, which is a prerequisite for the reduction of pores, thus enhancing the mechanical properties. The range of particle sizes is quite broad—from less than 100 nm to greater than 100 μm. However, the 4-sieve particle-size distribution (henceforth: PSD), which was borrowed from soil mechanics, is of great importance. Sieving is one of the oldest techniques for powder separation (based on size or some other physical characteristic) still in use today. It is among the most widely used and least expensive methods due to its relative simplicity, low capital investment, high reliability and the low level of technical expertise required for the determination of the PSD for a broad range of sizes. There are both dry and wet sieving processes. Typically, wet sieving is used for the analysis of particles finer than $\sim$200 mesh (75 μm). For particle-size analysis, one can consult Special Publication 960-1 of the National Institute of Standards and Technology (henceforth: NIST).

Products used in ceramic or abrasive applications are generally manufactured from powders. The PSD has profound effects on the processing and functioning of these products, which include most oxides and minerals ranging from aluminum oxide to zirconium oxide. Laser diffraction, dynamic light scattering and acoustic spectroscopy have all been successfully utilized to characterize ceramic materials.

It has been mentioned that particle size affects densification, which is a prerequisite for the reduction of pores, thus enhancing mechanical properties. The effect of pores in alumina serves as an example of the direct influence of densification which is influenced by particle size. Figure 2.24 shows flexural strengths following subjection to varying degrees of densification. In addition, changes in Young's modulus may be seen in Fig. 2.25. Changes occurring with different degrees of densification are expressed by the two relations given below: Eq. (2.11), suggested by Lam et al. [30] and Eq. (2.12), its modification given by Mangalaraja et al. [35]:

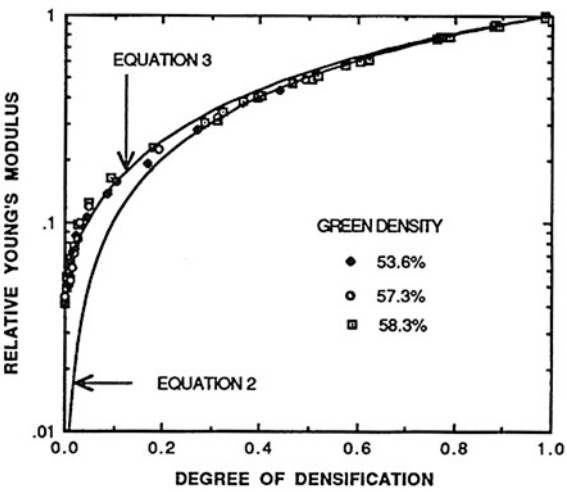

Fig. 2.25 Experimental Young's modulus data of high purity alumina for three different green densities expressed by the theoretical expressions mentioned above [5]. With kind permission of John Wiley and Sons

$$\frac{E}{E_0} = \left(1 - \frac{P}{P_g}\right) \tag{2.11}$$

and

$$\frac{E - E'}{E_0 - E'} = \left(1 - \frac{P}{P_g}\right) \tag{2.12}$$

As in the case of flexural strength, variation of the Young's modulus with the degree of densification increases during the initial stages of sintering.

In the above equations, E and E′ are Young's modulus values of the porous and the theoretically dense materials, respectively, and P is the fractional porosity (not load). The subscript g refers to the green body. The right-hand side of the equation represents the degree of densification. In Eq. (2.12), E′ is the Young's modulus at the onset of densification. The increase in strength properties, even with minimum densification, is an indication that strength property improvements may be made by controlling the sintering mechanism and the geometry of the particle structure.

Figure 2.26 shows the apparent porosity versus the average grain size of ceramic specimens sintered at ∼1340 °C. These specimens were prepared from magnesite and bauxite by means of an in situ pore-forming technique.

In general the size of the pores depends, among other factors, on the particle size of the aggregate. Particle size is the most important parameter in the production of ceramic products; it must be optimized to ensure that the desired mechanical and physical properties are achieved. The majority of ceramic products are manufactured by the process of slip casting in a mold. Maintenance of the desired PSD requires control of the dispersion stability of the ceramic slip. Like all ceramic materials and castables, in alumina refractories a proper PSD is of importance,

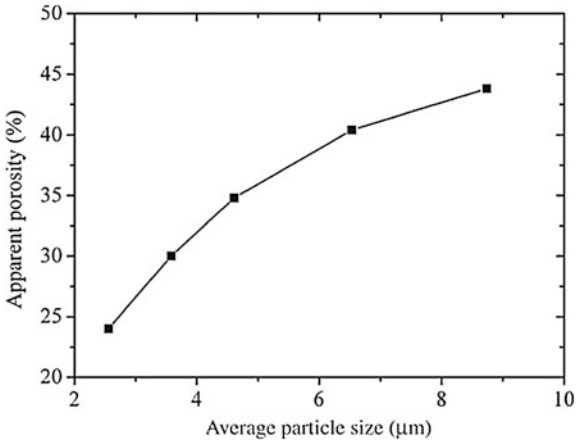

Fig. 2.26 Apparent porosity of specimens sintered at 1340 °C [50]. With kind permission of Professor Wen Yan

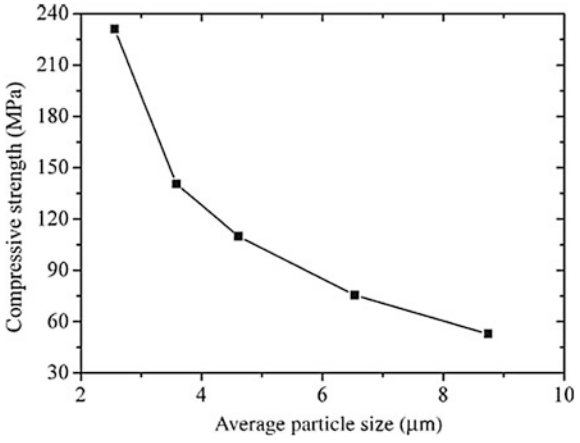

Fig. 2.27 Compressive strength of sintered specimes versus average particle size sintered at 1340 °C [50]. With kind permission of Professor Wen Yan

rather than using a single-sized component. This helps to create better packing, compared to the use of mono-sized particles. Besides influencing packing, PSD effects flow, apparent porosity and, hence, the strength of castables. Some research has been done to discover the relationship between particle size and physical properties. Figure 2.27 shows compressive strength versus average particle size.

Having established that the size of the pores depends on particle size, some other examples may now be considered, in which the effect of grain size is expressed in terms of pore density. In shell casting, ceramic molds are often used. Previous studies have indicated that zirconia is one of the least reactive materials and apparently holds promise as a mold refractory material, viable for metallurgical processing and the investment casting of TiAl alloys [15]. An important factor in zirconia mold properties is the role played by PSD on the packing. Information on this experimental procedure and the effect of PSD on zirconia mold properties may be found in the original paper of Chen Yan-fei et al. [15] FG,

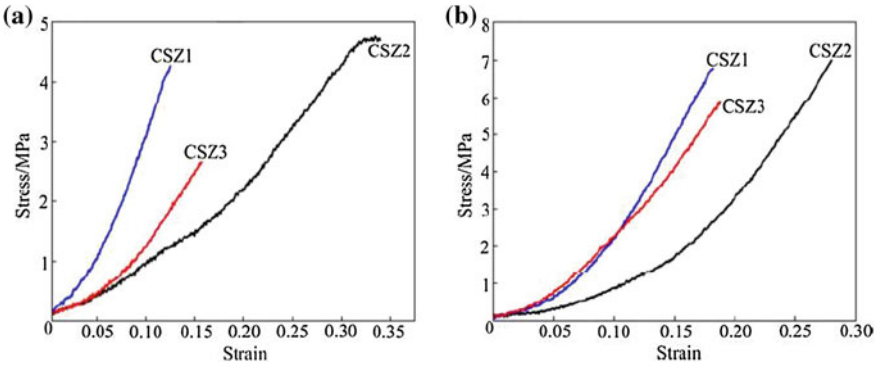

Fig. 2.28 Stress–strain relations for the CSZ1, CSZ2 and CSZ3 specimens; **a** green stage, **b** sintered [15]. With kind permission of Elsevier

uniform, sintered microstructure is obtained from slurries with median PSD and optimal viscosity, which facilitate particle arrangement and a structure with good packing. The mechanical properties of these molds were evaluated at RT by three-point bend tests of green and sintered (950 °C for 2 h) aggregates. Instron was used for the constant load test on five samples. The bending is given as:

$$\sigma_w = \frac{3FL}{2ah^2} \tag{2.13}$$

where F is the fracture load, L is the span length, and a and h are the width and thickness of the sample fracture area, respectively. Equation (2.13) is basically the same relation given in Eq. (1.122) from Chap. 1, Sect. 1.9, which was then given as:

$$\sigma_f = \frac{2P\frac{L}{2}c}{\frac{2tc^3}{3}} = \frac{3PL}{2tc^2} \tag{1.122}$$

In 1.122 P = F, t = a and $c^2 = h^2$.

The load–deflection relation in Eq. (2.13) may be expressed in terms of the stress–strain relation as:

$$\varepsilon = \frac{6h\delta}{L^2} \tag{2.14}$$

where ε and δ are the strain and deflection, respectively. Figures 2.28a and 2.28b are the stress–strain curves, in accordance with Eqs. (2.13) and (2.14) at the green and sintered stages, respectively, for the CSZ1, CSZ2 and CSZ3 specimens having different PSDs. It is interesting to compare the aggregates of these samples in the green stage and post-sintering (see Figs. 2.29 and 2.30). The PSDs of the powders used for these zirconia mold preparations appear in Fig. 2.31, showing that the median particle diameters are 20, 30 and 40 μm, respectively.

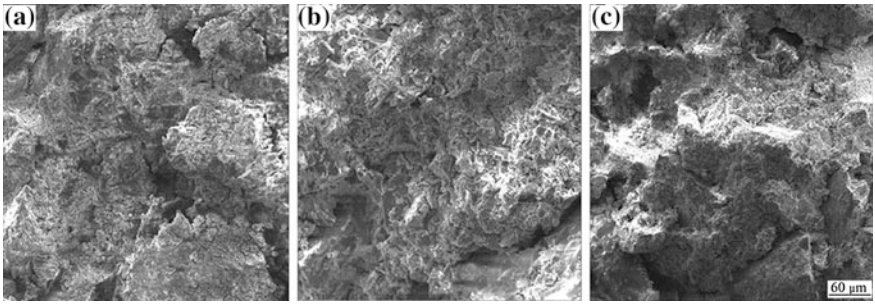

Fig. 2.29 Morphologies of fracture surfaces of green zirconia ceramic moulds with different PSDs: **a** CSZ1; **b** CSZ2; **c** CSZ3 [15]. With kind permission of Elsevier

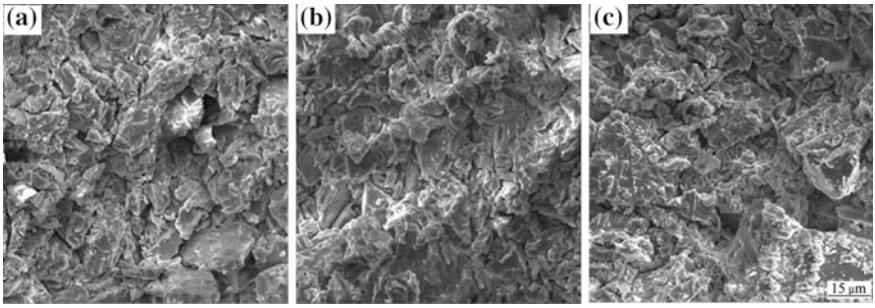

Fig. 2.30 Morphologies of fracture surfaces of sintered zirconia ceramic moulds with different PSDs: **a** CSZ1; **b** CSZ2; **c** CSZ3 [15]. With kind permission of Elsevier

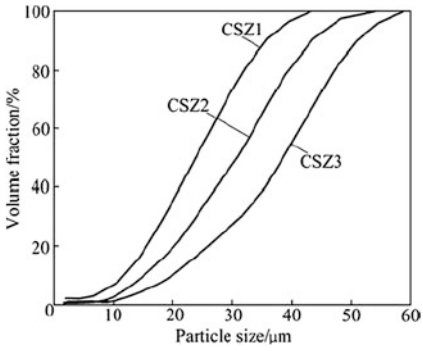

Fig. 2.31 Particle size distributions of zirconia powders [15]. With kind permission of Elsevier

The particle morphologies of the zirconia powders observed by scanning electron microscope (henceforth: SEM) are shown in Fig. 2.32.

Observations indicate that particle morphology and PSD greatly influence the quality of slurries in the reproduction of details and thin sections of ceramic molds. Consequently, good cast-metal quality may be obtained. It is clear from the results

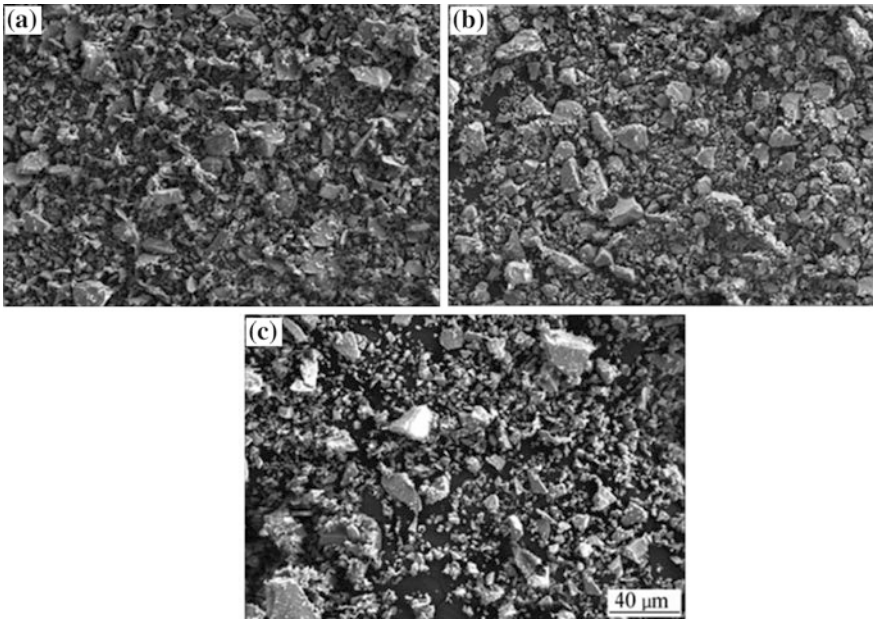

Fig. 2.32 SEM micrographs of zirconia powder: **a** CSZ1; **b** CSZ2; **c** CSZ3 [15]. With kind permission of Elsevier

that the surface roughness of castings is directly related to the fineness of the investment powders. Decreasing the size of powders causes the formation of extremely small pores in the zirconia ceramic mold which prevents the deeper penetration of molten TiAl into these cavities under the same hydrostatic or centrifugal pressure and, thus, improving surface quality. Thus, pore size, in particle-size-dependent zirconia molds, greatly influences casting quality; the finer the particle size, the smaller the pore diameter in the ceramic mold. The relation between the zirconia powder characteristics determines the resulting mechanical properties of the ceramic molds. The bend strength of zirconia ceramic molds is directly related to the PSDs in the green and sintered ceramic (bar-shaped) specimens.

2.1.2 Ductile Ceramics at Low or Ambient Temperatures

This section deals with the features of ductile ceramics and, in some cases, the modifications in composition that induce ductility at low temperatures, as well as additives to base ceramics, such as metals, which also promote ductility.

Polycrystalline ceramics are of great interest for specific industrial applications, but the primary drawback of using ceramic materials in structural applications is their inherent brittleness, which results from the strong bonding between the metallic and non-metallic components. In general, most ceramics are brittle and

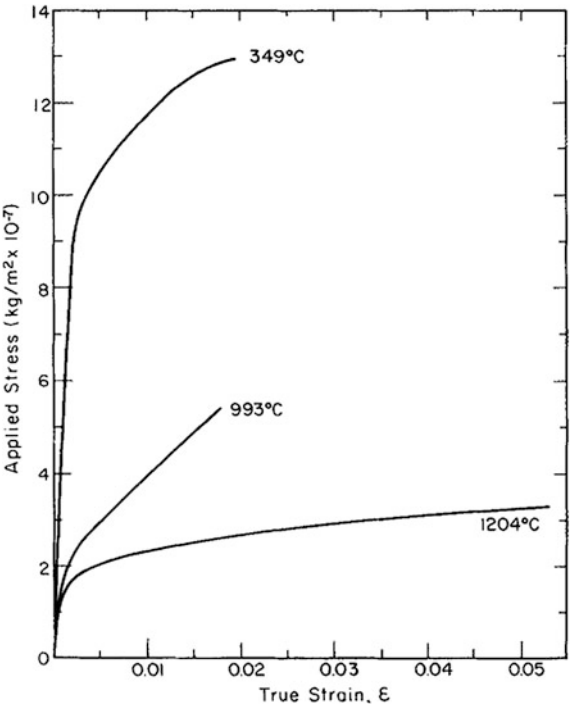

Fig. 2.33 Stress–strain curves for single crystals of MgO with a ⟨111⟩ loading axis [23]. With kind permission of Elsevier

various internal imperfections, such as porosity, reduce both strength and ductility. Due to the fact that most engineering ceramics are compacted from powders, the presence of some porosity is inevitable, which makes most ceramics very brittle. Furthermore, ceramics suffer from the presence of microcracks, which act as stress raisers. Generally, tensile stresses must be kept low, if sudden failure is to be avoided. Although the production of ductile polycrystalline ceramics (or other ionic solids) at RT has not yet been achieved in a satisfactory manner, it has been the objective of many research studies. Material purity is a contributing factor, though not necessarily a controlling one in governing the RT ductility of solids, in general, and of ceramics, in particular. Moreover, complications exist in polycrystalline ceramics, involving the presence of particles in the grain structure that may induce grain-boundary sliding, thus masking the possibility of real ceramic ductility in the absence of the contribution of grain-boundary sliding. Therefore, attempts have been made to study ductility in single crystals, in which a contribution from grain boundaries is ruled out.

A typical and much studied example of ductility in single crystals is MgO. Parker et al. [6] were the first to suggest that single crystals of MgO could be deformed at RT. Ever since the probability of RT ductility was confirmed, much attention has been given to evaluate the factors that affect such ductility and the mechanical properties of this structure. In addition to the other effects, crystal orientation also affects the deformation of single crystals. Figure 2.33 relates

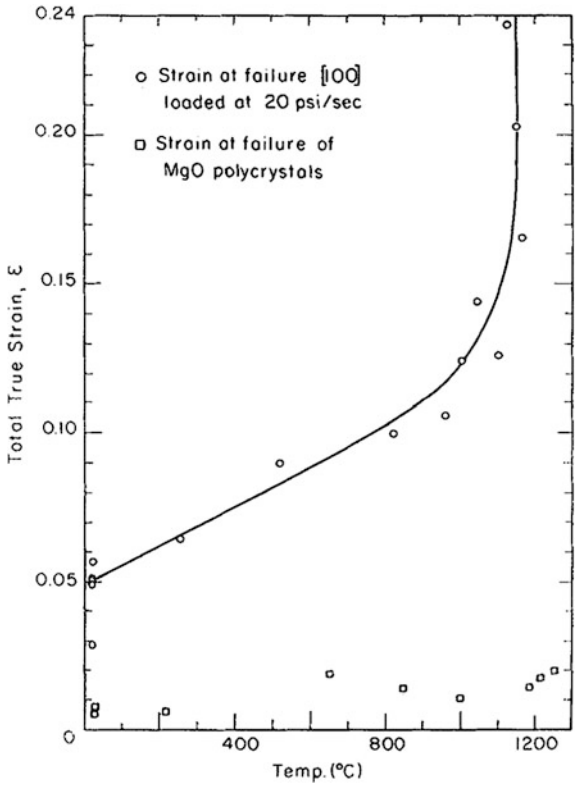

Fig. 2.34 Total strain versus temperature for single-crystal MgO with a ⟨100⟩ loading axis and for polycrystalline MgO [23]. With kind permission of Elsevier

applied stress to true strain at three temperatures. The lowest temperature in this figure is 349 °C, not strictly RT. However Fig. 2.34 also shows RT ductility (strain). Figure 2.35 shows stress–strain curves for small-grained polycrystalline material. When this polycrystalline material was yielded at RT using the Instron machine, yielding was followed by a decrease in stress at an increasing rate until final fracture occurred.

The temperature dependence of the bulk yield stress of the small-grained polycrystalline specimens is included in Fig. 2.34 for comparison with the single-crystal results. Note that the RT strain of the small-grained polycrystalline MgO is 0.005. Also notice that the loading axis orientation is ⟨100⟩ and not ⟨111⟩ as in Fig. 2.33. Figure 2.36 shows the variation with temperature of yield stresses for MgO single crystals with various loading axes. The yield-stress variation is also indicated for polycrystalline MgO. Typical behavior for single crystals loaded with a ⟨111⟩ axis at RT failed without plastic deformation.

A slip-band structure may be seen in Fig. 2.37, showing specimens deformed at RT and at 1240 °C. This band structure is similar to the dislocation band structure revealed by hot etching {100} faces of a ⟨111⟩ specimen just yielded at about 650 °C and then air-quenched (Fig. 2.38). In Fig. 2.34, the RT true strain at failure

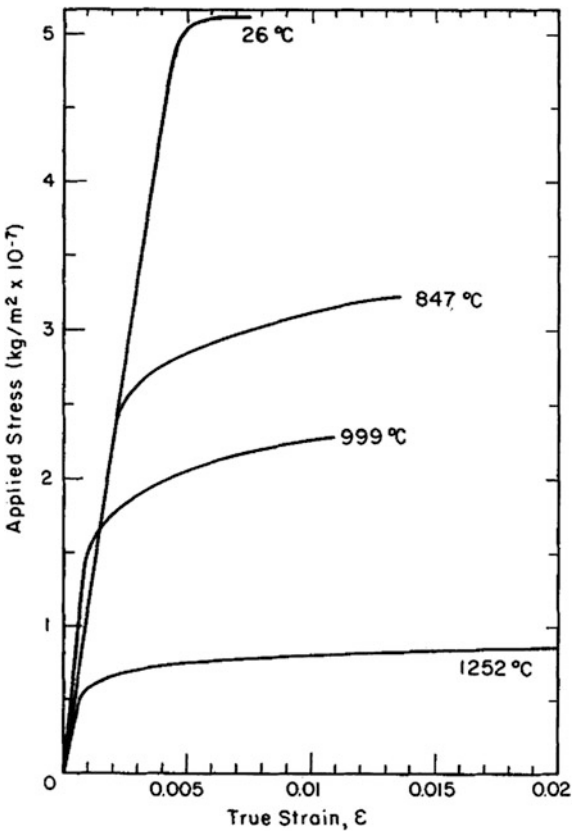

Fig. 2.35 Stress–strain curves far small-grained polycrystalline MgO [23]. With kind permission of Elsevier

of [100] loaded specimen at 20 psi/s was about 0.05. The polycrystalline MgO at RT had a strain at fracture of about 0.6 %, as seen in Fig. 2.34 and was about 2 % above 600 °C. The observed poor ductility of the polycrystalline MgO is attributed to cleavage fracture, slip non-uniformity and a lack of five independent slip systems, which is a requirement for polycrystalline ductility according to Taylor [45]. Above 600 °C, slip can occur on the {100} ⟨110⟩ slip system. At higher temperatures, stress-induced climb and high dislocation mobility inhibit cleavage fracture. Surface effects are extremely important and good ductility can be obtained only with specimens having carefully prepared, chemically polished surfaces. Thus, the ⟨110⟩ slip systems provide the additional slip systems necessary to satisfy Taylor's criterion. It was also found that MgO single crystals are ductile at RT and elongation values in excess of 10 % were obtained regularly [6]. Elongations of as much as 20 % on the tension side of a single-crystal bend-test specimen have also been reported. High purity is essential. Thus, purity and environmental effects play major roles in brittleness [41].

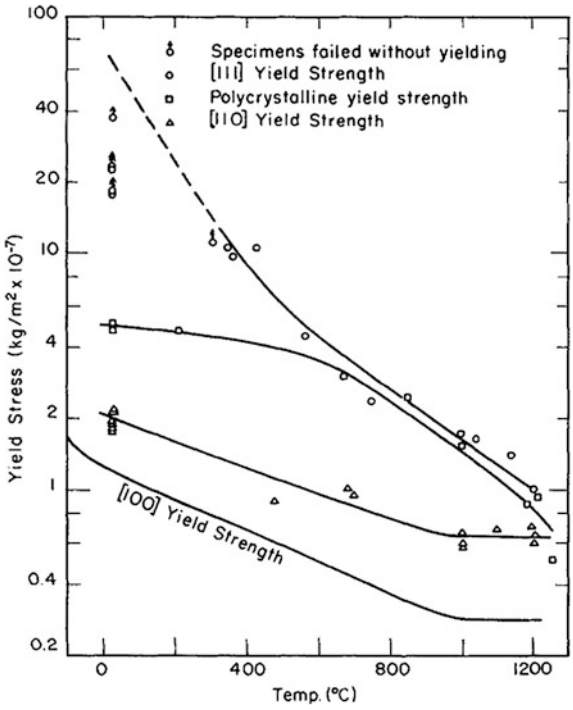

Fig. 2.36 Yield stress versus temperature for single-crystal and polycrystalline MgO [23]. With kind permission of Elsevier

Studies on single crystals, bicrystals and polycrystalline materials of MgO have shown that the strength of magnesium oxide depends on the availability of mobile sources. Research on single crystals has shown that the mechanical properties of magnesium oxide fall into two categories, namely, they are either extremely strong and elastic in the complete absence of mobile dislocation sources or relatively weak and ductile in their presence [43]. The mobility of a dislocation depends on a number of factors, such as crystal structure, bond character, temperature and microstructure. In pure magnesium oxide at RT, dislocations are very mobile at comparatively low stresses [42]. Changing the microstructure, possibly by alloying, the mobility of dislocations may be reduced and an increase in strength may be achieved.

As indicated above, the effects of impurities and surface reactions with components of the air exert control over ductility. It was predicted by researchers that a class of materials, normally considered brittle (i.e., ionic solids having cubic crystal structures) would possess a degree of ductility. Experiments performed on ionic materials indicate that face-centered cubic and body-centered cubic ionic materials can exhibit a considerable amount of ductility under controlled conditions, such as induced by impurities and surface effects. For instance, the ductility of MgO is shown in Fig. 2.39.

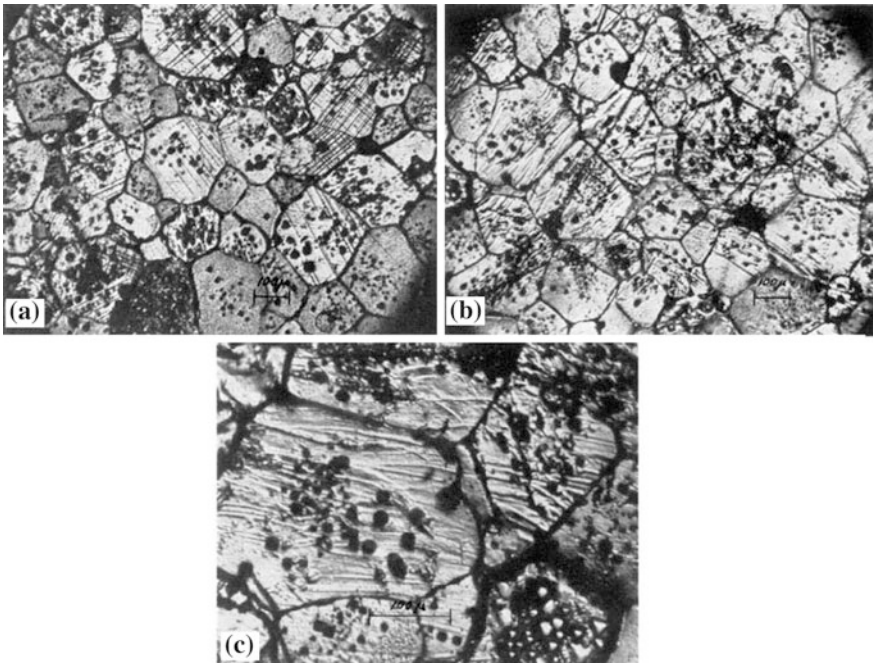

Fig. 2.37 **a** Etched grains of polycrystalline MgO deformed at room temperature, X95; **b** deformed at 1240 °C, X95; **c** deformed at 1240 °C, X190 [23]. With kind permission of Elsevier

Fig. 2.38 Etched {100} ⟨110⟩ slip bands (X75) [23]. With kind permission of Elsevier

The stress–deflection curve for a MgO single crystal is indicated in Fig. 2.40. To eliminate the environmental effect, these specimens were cleaved and tested under oil. The base material was of commercial grade, thus the crystals were impure,

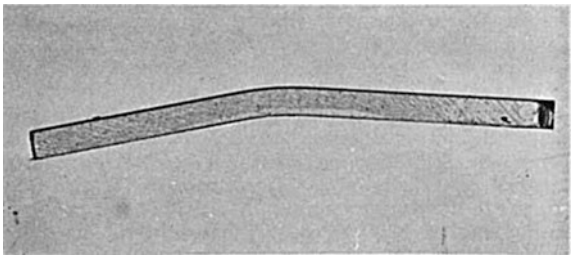

Fig. 2.39 MgO single crystal which was bent in air at room temperature [20]. With kind permission of John Wiley and Sons

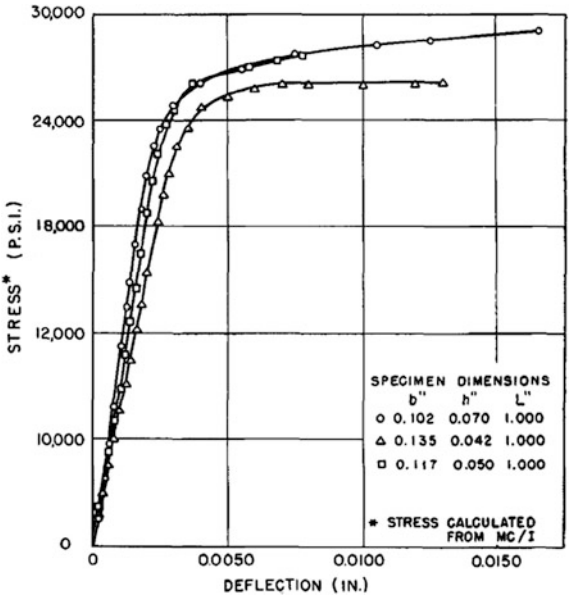

Fig. 2.40 MgO cleaved under oil, stored 48 h, and then tested under oil [20]. With kind permission of John Wiley and Sons

containing $\sim 1/2$ % or even more of foreign material (mostly silica). Nevertheless, the amount of elongation on the tension side of the specimens varied from 0 to 20 %, with an average of perhaps 5 % for the batch tested. In Fig. 2.40, three typical stress–deflection curves for MgO are seen. Undoubtedly, the variation in ductility was due, in part, to variation in purity. The effect of impurities and ambient gases, such as O or N, are assumed to be associated with the dislocation-impurity interaction. O or N can diffuse from the surface into the interior of the ceramic, acting like inherent impurities. It is well known that the reaction of the impurities with the dislocations and their pinning form Cottrell-like atmospheres. Dragging dislocations with their atmospheres and their immobilization are dependent on the amount of impurities and the amount of locks formed by impurity-dislocations interactions. Dislocation sources may have been activated by the high local stresses required to activate the motion of the dislocations having impure atmospheres. Eventually, when sufficient atmospheres form, the dislocation is immobilized and cleavage sets in. Thus, the free motion of dislocations gradually becomes more

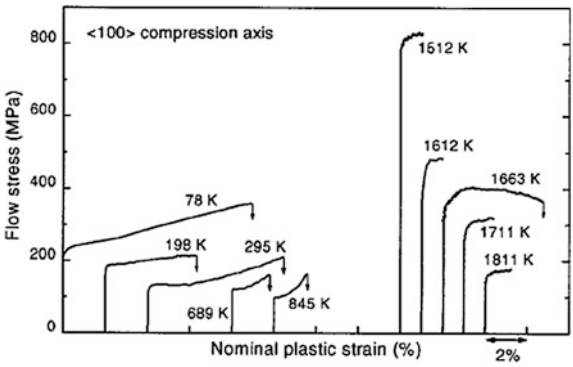

Fig. 2.41 Stress–strain curves of $SrTiO_3$ at different temperatures (arrows indicate load release) [13]. With kind permission of John Wiley and Sons

difficult and ductility becomes restricted, requiring higher stresses. The effect of embrittlement by impurities or by ambient gases depends on their amount.

One interesting case is that of the ceramic $SrTiO_3$, which belongs to the class of ceramics having a perovskite structure. This ceramic is expected to fail in a brittle manner at low temperatures, but, surprisingly, it was found to exhibit plastic behavior when deformed by compression in the range of 78–1050 K. Above this temperature, in the 1500–1800 K range, it behaved as a brittle material [13]. Such materials are often used as substrates for electronic devices for high-temperature superconductors. Therefore, there is a need to obtain information about the mechanical properties of $SrTiO_3$. Single crystals of $SrTiO_3$ were tested by compression in the $\langle 001 \rangle$ orientation at 78–1811 K. Figure 2.41 displays representative curves of the true stress versus the nominal plastic strain in $SrTiO_3$ specimens that were deformed at 78–1811 K.

Several features may be observed in Fig. 2.41 at several temperatures:

(1) The stress at the beginning of plastic deformation is weakly dependent on temperature;
(2) The stress plateau of plastic deformation, being the most pronounced at 296 K, decreases with increasing temperature and;
(3) The work-hardening rate after the short plateau increases with increasing temperature.

The most striking feature of the stress–strain curve at RT is the extended plastic deformation, reaching a plastic compressive strain of up to 8 % before fracture. At 78 K, a specimen can be plastically strained to 9 % before fracture. Figure 2.42 shows the two side faces of a specimen that has been deformed to 3 % at RT in transmitted polarized light. The bands of birefringence lie at an angle of 45° to the [001] compression axis. These structures are typical of plastically-deformed specimens at temperatures below 900 K; above 1500 K, no such structures can be detected within the deformed, transparent samples, since no plastic deformation has taken place. Figure 2.43 suggests that the temperature range under investigation may be subdivided into four regimes: (i) regime I ($T \leq 300$ K), the low-temperature regime, where σ_c (critical flow stress) decreases as the temperature

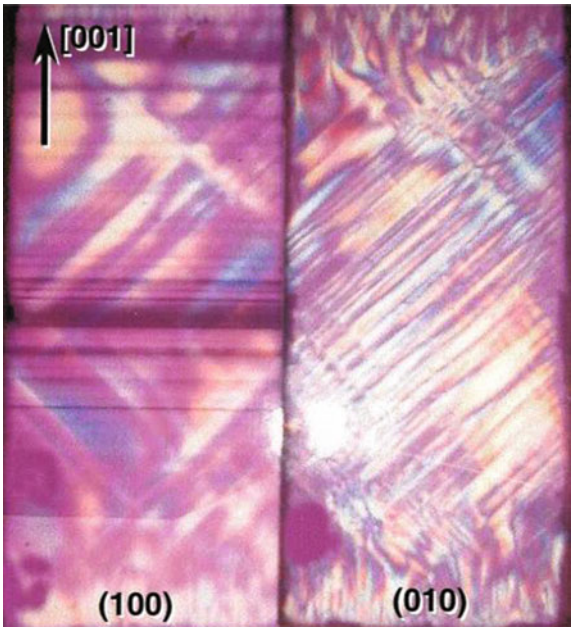

Fig. 2.42 Polarized-light micrograph showing single-crystal $SrTiO_3$ after 3 % plastic deformation at RT [13]. With kind permission of John Wiley and Sons

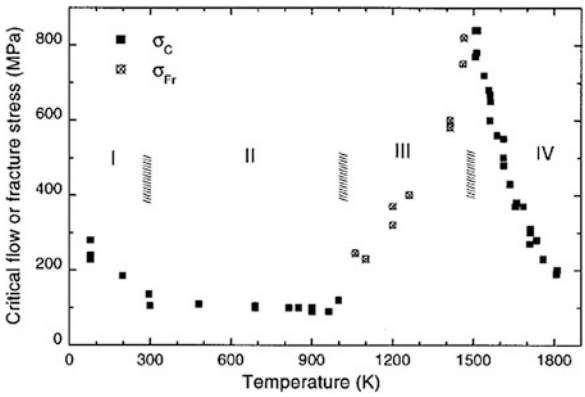

Fig. 2.43 Critical flow stress (σ_c) and fracture stress (σ_{Fr}), as a function of temperature [13]. With kind permission of John Wiley and Sons

increases and high ductility is observed; (ii) regime II (T = 300–1050 K), which is characterized by an almost-constant σ_c value and ductile behavior decreases as the temperature increases; (iii) regime III (T = 1050–1500 K), which is characterized by complete brittleness of the specimens, but an increase in σ_{Fr} (fracture stress) is observed with increasing temperature; (iv) regime IV (T = 1500–1811 K), where ductility occurs again, but σ_c rapidly decreases if the temperature is increased. Thus, a 'two-directional' transition phenomenon-a ductile–brittle-ductile transition—is observed in these ceramics.

It can be summarized that a class of ceramics materials, normally considered brittle could posses a degree of ductility depending on the production technique,

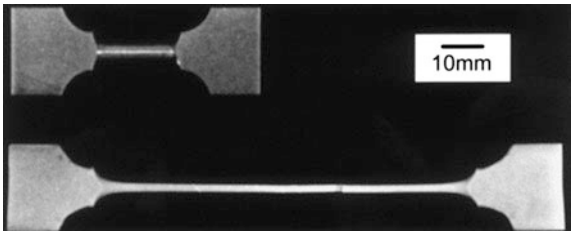

Fig. 2.44 Undeformed and superplastically deformed Si_3N_4. An elongation over 470 % is noted [47]. With kind permission of Elsevier

and among the many factors the impurity concentration exerts control over the degree of ductility. The restriction to use ceramic materials at low temperature by the transition from ductile behavior to brittle fracture can thus be overcome in cases when production occurs under strict controlled conditions.

2.1.3 Superplasticity in Ceramics

2.1.3.1 Introduction

A superplastic phenomenon occurs in solid crystalline materials, including ceramics, and is a state in which the material may be deformed before fracture and may reach large strains, well above 100 %, often even in the range of 200–500 %. Figure 2.44 shows superplastic behavior in Si_3N_4 with a 470 % elongation.

This usually occurs at high, homologous temperatures of about 0.5 T_m, where T_m is the absolute melting temperature. However, often a superplastic state is found in metals and alloys even at RT. An essential feature of materials exhibiting superplastic behavior is their fine grains. Superplastic materials may be thinned down, usually in a uniform manner, before breaking, without neck formation, unlike ductile metals, where necking is a common feature before fracture sets in. Two-phase ceramics seem to be desirable for superplasticity, since the second-phase particles are finely dispersed to pin the grain boundaries, thus maintaining the FG structure. The particles in superplastic materials are thermally stable. In addition, these ceramics must be strain-rate sensitive, with a value >0.3. Recently, superplastic behavior was also observed in iron aluminides with coarse grain structures. It is believed that this is due to recovery and dynamic recrystallization. Some relate superplasticity to grain boundary sliding [31]. Most of the reports consider ZrO_2 (zirconia) as a typical superplastic ceramic. New developments have also been achieved in the superplasticity of Si_3N_4 and SiC.

2.1.3.2 Oxide Superplastic Ceramics

As previously indicated, zirconia is a typical superplastic ceramic and was among the first oxide ceramics to be studied. As early as 1986, Wakai et al. studied

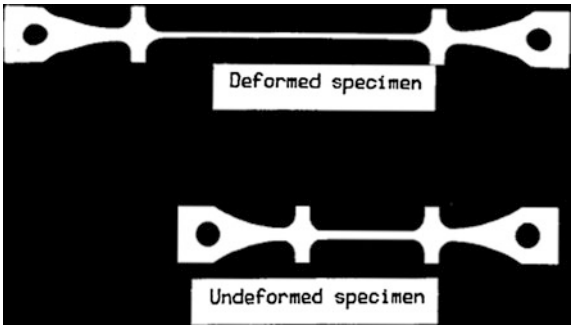

Fig. 2.45 Superplastically elongated specimen of Y-TZP at 1450 °C [48]. With kind permission of Professor Wakai

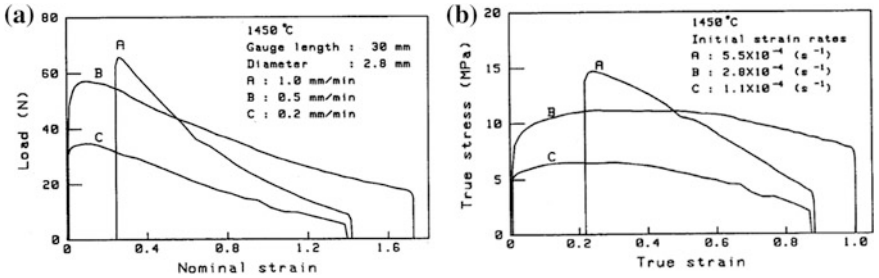

Fig. 2.46 **a** Load-nominal strain under constant displacement rate; **b** estimated true stress–true strain curves assuming a uniform deformation without necking [48]. With kind permission of Professor Wakai

yttria-stabilized tetragonal zirconia FG polycrystals (henceforth: Y-TZP) in the temperature range of 1000–1500 °C. The grain size was ≤0.3 and the tensile experiments were performed at strain rates of 1.1×10^{-4}–5.5×10^{-4} s^{-1}. Over 120 % strain was obtained at 1450 °C. Furthermore, the interest in this ceramic is a consequence of its excellent bending strength and toughness. The yttria (3 mol percent) was in solid solution. Figure 2.45 illustrates the superplasticity observed in this alloy.

The Y-TZP specimen showed an elongation >120 %. It is compared with an undeformed specimen. The elongation in the gage length was uniform and no local necking was observed. These tests were performed at constant displacement in a universal tensile testing machine in air and at 1450 °C. The results of these tests are shown in Fig. 2.46. As usual, the true strain, ε_t, was obtained (see Chap. 1, Sect. 1.2.1) by using:

$$\varepsilon_t = \ln \frac{l}{l_0} = \ln\left(1 - \frac{\Delta l}{l_0}\right) \tag{1.9}$$

In the above, l and l_0 are the elongated and original gage lengths, respectively. The true stress is related to the true strain by:

$$\sigma_t = \sigma \exp(\varepsilon_t) \tag{2.15}$$

where the nominal stress is the ratio of the load, P, to the original cross-section of the specimen, A_0, i.e., $\sigma = (P/A_0)$.

2.1.3.3 Other Non-oxide Superplastic Ceramics

Superplasticity is not limited to zirconia-type ceramics. Other ceramics have also been found to exhibit superplasticity, such as nitrides or carbides. Representative examples are Si_3N_4 and SiC. In these cases, superplasticity occurs in single-phase ceramics. Section 2.1.3.1 (i) A superplasticity of $\sim$ 470 % in Si_3N_4 (Fig. 2.44) has been mentioned above.

Superplasticity is one of the common properties of FG ceramics at elevated temperatures. Superplastic forming and strengthening by superplastic forging are applicable to a wide range of ceramics, including oxides and non-oxides. Zhan et al. [51] have studied the superplastic behavior of FG β-silicon nitrides (with 5 wt% Y_2O_3) under compression in the temperature range 1450–1650 °C at various strain rates. It was found that β-Si_3N_4 can be deformed at high strain rates ($\sim 10^{-4}$–10^{-3} s^{-1}) in a range of temperatures and at pressures of 5–100 MPa. No strain hardening occurs even during slow deformation. Beside Eqs. (1.9) and (2.15), the initial strain rate may be expressed as:

$$\dot{\varepsilon} = \frac{\dot{l}}{l_0} \tag{2.16}$$

Here, $\dot{l}$ is a constant. The immediate strain rate is expressed as:

$$\dot{\varepsilon} = \dot{\varepsilon}_0 \exp(-\varepsilon) \tag{2.17}$$

The corrected flow stress is given by:

$$\sigma_c = \sigma_0 [\exp(\varepsilon)]^{\frac{1}{n}} \tag{2.18}$$

For the corrected flow stress the stress exponent, n, must be known and is given as:

$$\dot{\varepsilon} = A\sigma^n \tag{2.19}$$

A typical, corrected true stress-true strain curve is shown in Fig. 2.47, together with the uncorrected curve. The effect of the strain rate at 1550 °C during a compression test is seen in Fig. 2.48. After the initial transient state, a steady state is reached for all the strain rates. The true strain rates are based on the corrected data. As can be seen, no strain hardening occurred in these tests, even at low strain rates, unlike other cases in which pronounced strain hardening has been observed. In those cases, the starting powder was α-Si_3N_4, rather than β-Si_3N_4. The strain hardening was attributed to microstructural changes during deformation, such as dynamic grain growth and α-to-β phase transformation. However, no shape change

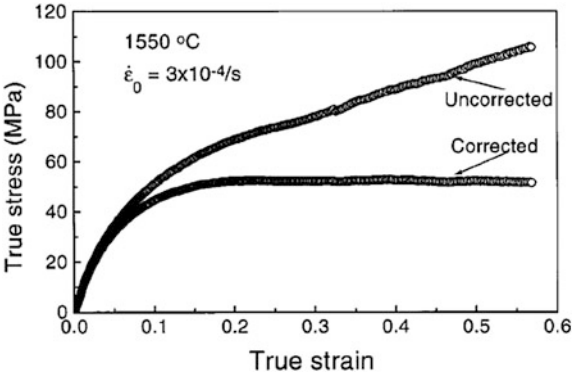

Fig. 2.47 Typical correction curve for a compression test at 1550 °C and an initial strain rate of 3×10^4/s, in the as-hot-pressed β-Si_3N_4 [51]. With kind permission of John Wiley and Sons

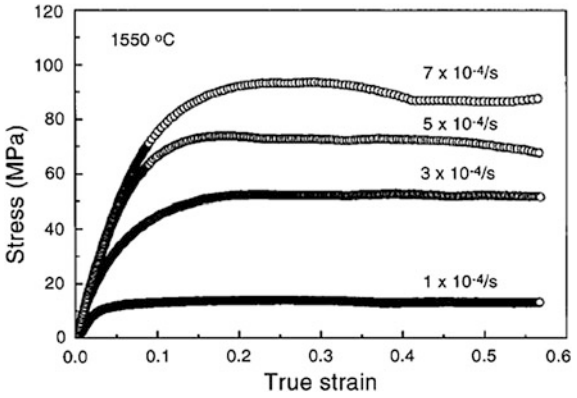

Fig. 2.48 Compressive stress–strain curves for various strain rates of the as-hot-pressed Si_3N_4 at 1550 °C [51]. With kind permission of John Wiley and Sons

occurred in the present material, due to the uniform PSD of the starting powder and the absence of an α-to-β phase transformation, as illustrated in Fig. 2.49.

The mechanism that controls the deformation rate at high temperatures, i.e., the plastic flow, may be expressed (constitutive equation) by:

$$\dot{\varepsilon} = \frac{A\sigma^n}{d^p} \exp\left(-\frac{Q}{RT}\right) \tag{2.20}$$

where $\dot{\varepsilon}$ is the strain rate, σ the flow stress, A is a temperature-dependent constant, d the grain size, n and p the stress and grain-size exponents, respectively, and Q the activation energy for flow.

In order to use Eq. (2.20), the stress exponent, n, must be determined. A plot, according to Eq. (2.19), expressed on a logarithmic scale at various temperatures provides the values of n, as shown in Fig. 2.50. The slopes of these curves give the values of n at the temperatures indicated. The initial flow stress regions were ignored and only the quasi-steady-state part of the flow stress is plotted in Fig. 2.50. Note that the values of n that barely change with temperature are $\sim$1–1.4.

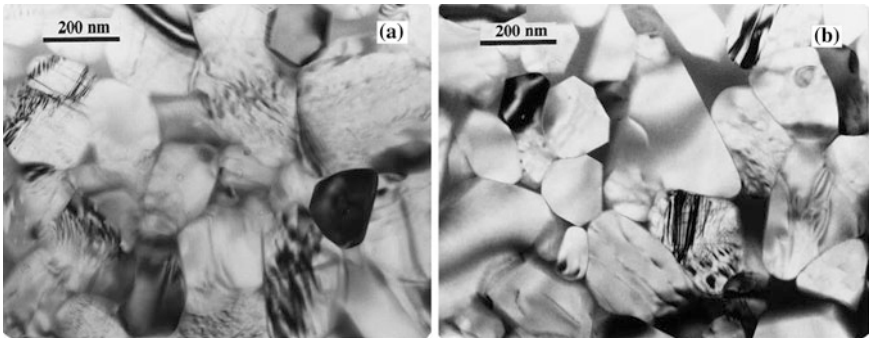

Fig. 2.49 TEM photographs of: **a** an undeformed sample and **b** a deformed sample at 1600 °C, with a true strain of −1.1, showing no dynamic grain growth [51]. With kind permission of John Wiley and Sons

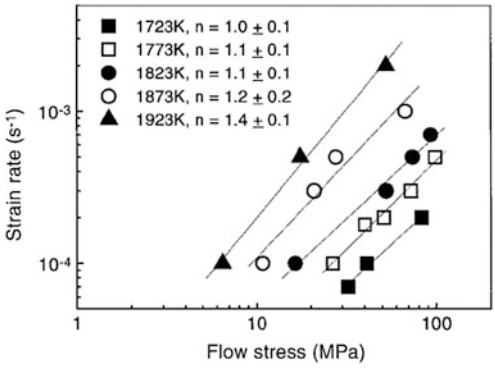

Fig. 2.50 Strain rate versus stress at various temperatures, under compression (n = slope), in the as-hot-pressed β-Si_3N_4 [51]. With kind permission of John Wiley and Sons

The higher values of the stress exponent seem to occur at temperatures above 1823 K. The temperature dependence of the strain rate is shown in Fig. 2.51, where the strain rate is plotted against the reciprocal, absolute temperature. The activation energy, Q, calculated from the slopes of the lines in Fig. 2.51, are 344 ± 26 kJ/mol at 20 MPa and 410 ± kJ/mol at 100 MPa. High-resolution transmission-electron microscopy (henceforth: HRTEM) observations of materials, both before and after deformation, are shown in Fig. 2.52. Observe that most of the grain boundaries have a glass film, although some grain boundaries were free of such film. This indicates that the formation of glass film is dependent on grain-boundary orientation and whether they were perpendicular or parallel to the direction of the applied force and on grain orientation. Those boundaries oriented in parallel show wide films (Fig. 2.52a), whereas the film thickness on grain boundaries perpendicular to the applied load direction were smaller (Fig. 2.52b).

It was also mentioned above that some relate superplasticity to grain-boundary sliding (see, for example [31]). Guo-Dong Zhan et al. [51] report that grain-boundary sliding may also be the mechanism of superplasticity in Si_3N_4, in

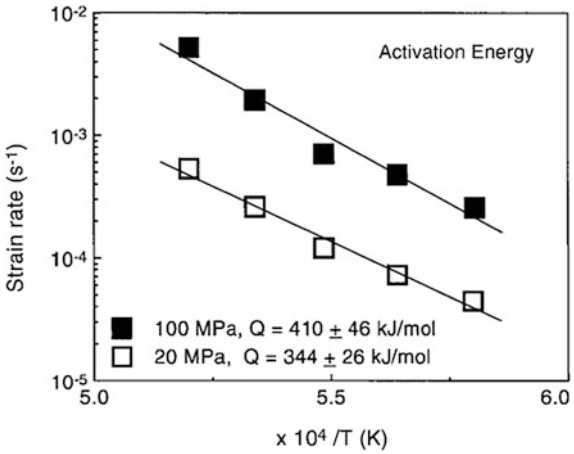

Fig. 2.51 Determination of activation energy for flow equation in the as-hot-pressed β-Si_3N_4 [51]. With kind permission of John Wiley and Sons

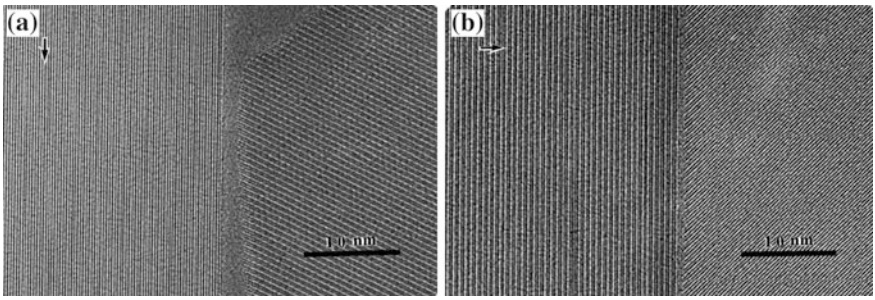

Fig. 2.52 Representative HRTEM photographs of boundaries oriented **a** parallel and **b** perpendicular to the applied load direction, indicating that the grain-boundary film thickness decreased after superplastic deformation, under compression ((→) applied stress direction during deformation) [51]. With kind permission of John Wiley and Sons

addition to grain rotation, accommodated by viscous flow. Furthermore, FG β-Si_3N_4 exhibits high grain-size stability against dynamic grain growth during sintering and deformation, a characteristic that satisfies the microstructural requirement for classic superplasticity. This kind of Si_3N_4 does not work-harden as do the other silicon nitrides discussed earlier.

2.1.3.4 Superplasticity in Carbides

'Superplasticity' is basically defined as the ability of a material to exhibit exceptionally large tensile elongation during stretching. In addition to oxides and nitride-like materials, some carbides also show large elongation and frequent

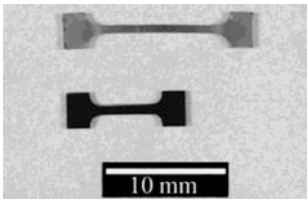

Fig. 2.53 HIPed B, C-SiC specimens before and after tensile deformation. The tensile test was conducted at 1800 °C, and at an initial strain rate of 3×10^{-5} s^{-1} in an argon atmosphere. The specimen deformed uniformly, and a superplastic elongation of 140 % was achieved [40]. With kind permission of John Wiley and Sons

superplastic behavior. For better familiarity with carbide behavior, this section will discuss SiC and FeC as exemplars.

(1) **SiC**

It is somewhat difficult to produce SiC without additives, because it is hard to obtain a dense material due to its low self-diffusivity and covalent nature. Thus, the role of the additives is to loosen or modify this bond structure. The most common additives are B and C [8]. B additives, for instance, provide superior mechanical strength at elevated temperatures. High superplasticity at a level of ~140 % has been observed in β-SiC doped with B or C and having a small grain size of 0.2 μm, fabricated by ultra-high hot isostatic pressure (henceforth: UH-HIP). The B segregated at the grain boundaries and apparently promoted grain-boundary sliding, one mechanism of superplasticity [4]. However, when liquid-phase sintering is the fabrication method and there is an amorphous phase at the grain boundary, rather than solid-phase sintering with no amorphous phase, it is easier to deform the product.

Basically, the degree of elongation depends on the additive. Thus, when 1 % B and 3.5 % free C are added to SiC fabricated by HIP at 980 MPa at a temperature of 1660 °C with an average grain size of 200 nm, a 140 % superplastic elongation is obtained at 1800 °C [40]. When β-SiC was produced by liquid-phase sintering, prepared with different oxynitride glasses in an N_2 atmosphere [4], the elongation was either 74 or 153 % at the initial strain rate of 1×10^{-5} s^{-1} at 2023 K under tension, depending on its composition (the additives forming the oxynitride glasses). Figure 2.53 compares specimens before and after deformation. A superplastic elongation of 140 % was achieved.

This specimen deformed uniformly. Stress–strain curves following HIP and hot-pressed B, C-SiC are shown in Fig. 2.54. The hot-pressed SiC was sintered under a pressure of 30 MPa at 2000 °C for 1 h and the average grain size was 2 μm. The B, C-SiC, after HIP, exhibited a superplastic elongation of >100 %, whereas the hot-pressed B, C-SiC fractured without significant plastic deformation. Thus, grain refinement was effective for obtaining superplasticity in SiC. HRTEM observation and electron energy-loss spectroscopy analysis revealed that there was no glassy phase at the grain boundaries, but boron segregation and carbon excess

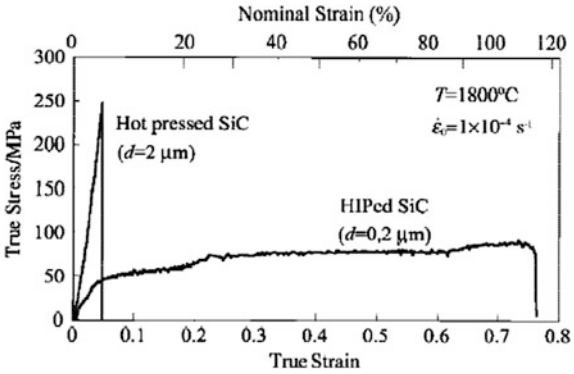

Fig. 2.54 Stress–strain curves of HIPed B, C-SiC and hot-pressed B, C-SiC. The tensile tests were conducted at 1800 °C and an initial strain rate of 1×10^{-4} s^{-1} in an argon atmosphere. HIPed, B, C-SiC exhibited superplastic elongation of 114 %, because of grain refinement. On the other hand, hot-pressed B, C-SiC fractured without plastic deformation [40]. With kind permission of John Wiley and Sons

Table 2.4 Chemical compositions and some properties of as-sintered materials [4] (with kind permission of Elsevier)

Material	Additives (wt%)					Grain size (nm)	Density (g/cm^3)	Sintering condition
	SiO_2	MgO	Al_2O_3	Y_2O_3	AlN			
SiC (G1)	3.78	0.981	1.17	2.13	0.936	260	3.15	2073 K 30 MPa 20 min in N_2
SiC (G2)			5.022	3.321	0.657	230	3.21	2073 K 30 MPa 15 min in N_2

were observed there. A small amount of oxygen segregation was also detected at the grain boundaries. However, the amount of segregated atoms was not enough to form an intergranular glassy phase, such as had formed in the experiments of Nagano et al. [4]. Yet, Wang et al. [49] indicate that the microstructure of the material, both before and after the superplastic deformation, retains the microstructural features of that material before its deformation.

In the work of Nagano et al. [4], the starting material was ultra-fine β-SiC powder with a particle size of $\sim$90 nm. The mixtures of SiO_2, MgO, Al_2O_3, Y_2O_3 and AlN were then rendered into oxynitride compositions by SiC ball milling in n-hexane. The SiC was mixed with 9 wt% oxynitride powders by SiC ball milling in n-hexane. The mixed powder was hot-pressed at 2073 K under a stress of 30 MPa in N_2. The chemical compositions and other properties of the sintered materials are shown in Table 2.4. Compression and tension tests at constant crosshead speeds were performed using a universal testing machine with a furnace at initial strain rates from 1×10^{-4} to 5×10^{-6} s^{-1} at temperatures ranging from 1973 to 2048 K in N_2. The degree of specimen deformation was evaluated from the displacement of the crosshead. Compressive and tensile directions were

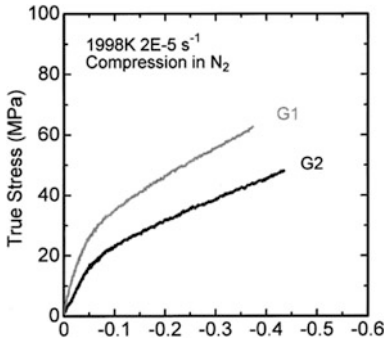

Fig. 2.55 True stress–true strain curves at 1998 K in compression tests [4]. With kind permission of Elsevier

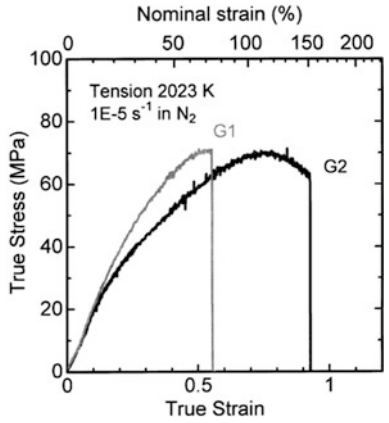

Fig. 2.56 True stress–true strain curves at 2023 K in tension tests [4]. With kind permission of Elsevier

perpendicular to the hot-pressing direction. The true stress–true strain curves at 1998 K are shown in Fig. 2.55. No cracks were observed in both compressed specimens. SiC (G1) showed higher flow stress and higher strain hardening in comparison with SiC (G2). The true stress–true strain relation is seen in Fig. 2.57. These tests were performed under tension. Strain hardening was observed in both specimens, i.e., SiC (G1) and SiC (G2). The SiC (G1) showed higher strain hardening and fractured at a 74 % elongation, while the SiC (G2) showed strain hardening to a 110 % elongation and then showed strain softening. The final elongation of SiC (G2) achieved was 153 % (Fig. 2.56).

These figures are based on Eqs. (2.16)–(2.19) and the strain-rate variation with temperature for the activation energy evaluation is based on Eq. (2.20). To use Eq. (2.20), the stress exponent, n, is required for various temperatures, which may be evaluated by using Eq. (2.19). Plots of this relation are shown in Fig. 2.57. HRTEM images at grain boundaries are shown in Fig. 2.58. An amorphous phase, from 1 to 2 nm, is evident in SiC (G1) and SiC (G2). However, some grain boundaries with no amorphous phases may be seen in SiC (G1). SEM photographs of the gauge portions of the elongated specimens are shown in Fig. 2.59. The cavitation damage of SiC (G1) after 74 % elongation was higher than that of SiC

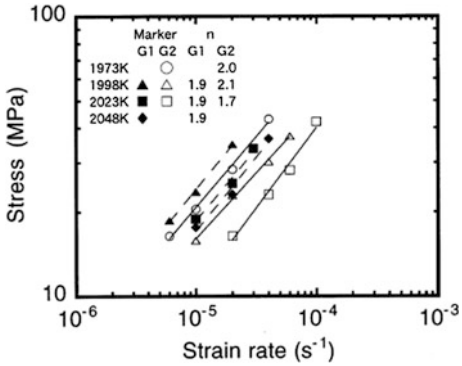

Fig. 2.57 Relationship between flow stress and strain rate [4]. With kind permission of Elsevier

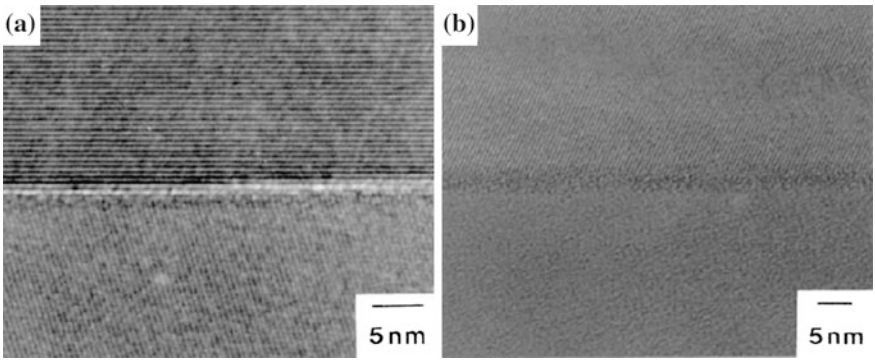

Fig. 2.58 HRTEM images at grain boundaries of **a** SiC(G1) and **b** SiC(G2) in as-sintered materials [4]. With kind permission of Elsevier

(G2) after 153 % elongation. On the one hand, the average grain sizes of SiC (G1) after 74 % elongation were 350 and 500 nm in the vertical and horizontal directions of the tensile axis, respectively; on the other hand, the average grain sizes of SiC (G2) after 153 % elongation were 300 and 430 nm in the vertical and horizontal directions of tensile axis, respectively. Most of the residual grain-boundary phase after 153 % elongation was at the triple points. The contribution of grain-boundary sliding to the total strain was calculated to be in the order of $\sim$76 % in elongated specimens of SiC (G1) and SiC (G2). Therefore, the critical deformation mechanism was thought to be grain-boundary sliding in both the SiC (G1) and SiC (G2) specimens. This being the case, the initial grain size of the as-sintered material, the grain-growth rate, the cavitation damage during deformation, the vaporization of the grain-boundary phase and the formation of crystalline phases at triple points are all significant factors for the improvement of superplastic deformation behavior in liquid-phase sintered SiC with an amorphous phase.

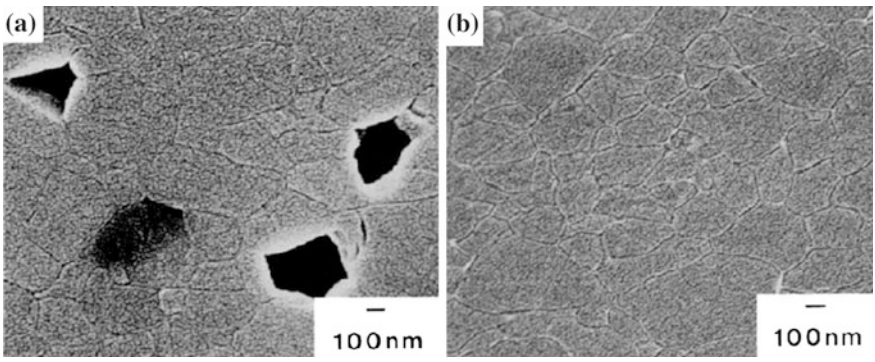

Fig. 2.59 SEM photographs of **a** 74 % elongated SiC(G1) and **b** 153 % elongated SiC(G2) [4]. With kind permission of Elsevier

(2) **FeC**

By now, it is clear that superplasticity is not restricted to a special group of materials. Even other carbides than the aforementioned SiC show superplasticity under certain conditions. Iron carbide, FeC, is such a carbide.

As indicated earlier, grain size, in general, is an important factor in superplastic phenomena and, in this regard, FeC is no exception. Thus, the processing of FeC for superplasticity studies is usually done on FG structures. As in other superplastic ceramic materials, a second phase is present. In the work of Kim et al. [28], for example, an iron-based second phase was added to the carbide. Strain-rate sensitivity is usually evaluated by testing for strain-rate changes. In such tests, a certain strain rate is applied to provide a strain creating isostructural conditions (similar structures), in order to obtain a stable grain size. While the strain rate is changed by specific strain-rate values, the stress must be recorded. A plot is made of flow stress versus strain rate on a logarithmic scale and from the slope of such curves, m, the strain-rate sensitivity is determined. It is necessary to perform such tests at various temperatures to determine the activation energy. The relation used is

$$\sigma = K\left[\dot{\varepsilon}\exp\left(\frac{Q_c}{RT}\right)\right]^m \tag{2.21}$$

The term:

$$\dot{\varepsilon}\exp\left(\frac{Q}{Rt}\right) \tag{2.21a}$$

is the Zener-Hollomon parameter (Dieter).

In Fig. 2.60, the flow stress is shown as a function of the strain rate-temperature parameter, $\dot{\varepsilon}\exp\frac{Q_c}{RT}$. The activation energy was evaluated as 200 kJ/mol. The strain-rate sensitivity exponent, m, is 0.5 as derived from the slope. K is a material

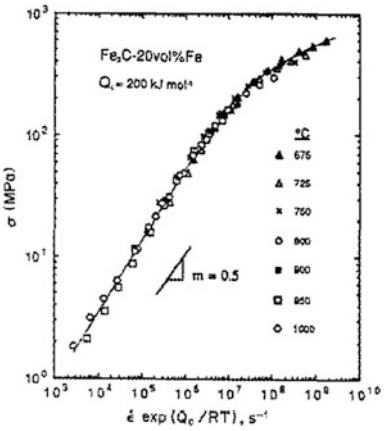

Fig. 2.60 The flow stress as a function of the strain rate-temperature parameter $\dot{\varepsilon}\exp\frac{Q_c}{RT}$ for a superplastic fine grained iron carbide (Fe_2C–20 % Fe) [28]. With kind permission of Elsevier

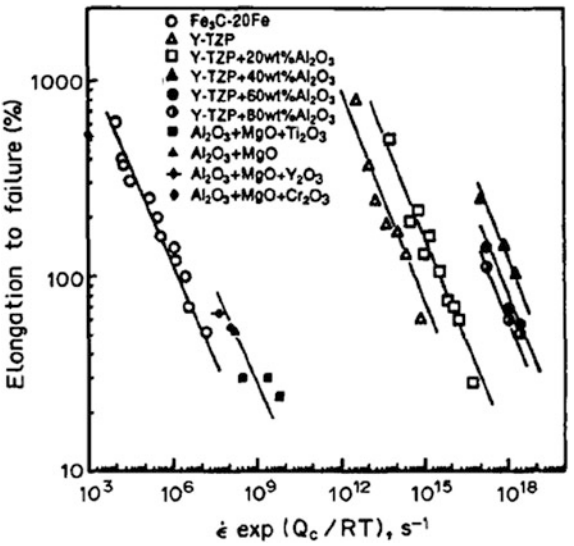

Fig. 2.61 Tensile ductility of fine-grained iron carbide as function of the Zener-Hollomon parameter is compared with some superplastic ceramics doped with various impurities. The strain rate sensitivity parameter is in the range m = 0.5–0.6 [28]. With kind permission of Elsevier

constant, which is a structural factor and a function of the modulus; $\dot{\varepsilon}$ is the steady-state strain rate and the other parameters are familiar.

The tensile ductility of various superplastic ceramics are compared with that of iron carbide in Fig. 2.61. All the curves show the same tendency, namely that tensile ductility decreases with increased strain rate-temperature, $\dot{\varepsilon}\exp\left(\frac{Q_c}{RT}\right)$. This decrease has been explained by grain growth. It is possible to superimpose all the superplastic ceramics data shown in Fig. 2.51 on a common curve when $\dot{\varepsilon}\exp\left(\frac{Q_c}{RT}\right)$ is multiplied by A, which is unique for each ceramic. The results are shown in Fig. 2.62.

Kim et al. [28], in their extensive work on superplasticity, classified materials on the basis of their elongations, defining 'superplasticity' as being ductility beyond 200 %. In accordance with their classification system: superplastic-like materials are those with elongations in the 50–200 % range; ductile ceramics have

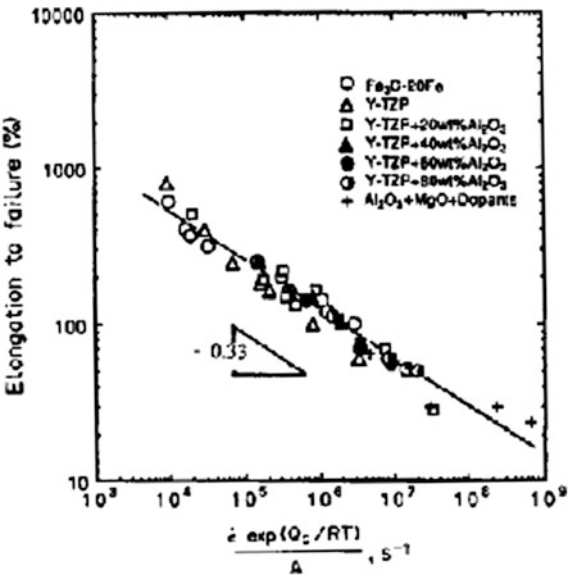

Fig. 2.62 Tensile ductility for fine-grained ceramics as a function of $\dot{\varepsilon}\exp\left(\frac{Q_c}{RT}\right)$ normalized by the material parameter [28]. With kind permission of Elsevier

elongations ranging from 3 to 50 %; and in brittle ceramics, elongations are below 3 %. They obtained tensile elongations as high as 600 % in FG iron carbide (Fe_3C–20 % Fe). The strain-rate sensitivity is an important parameter.

In an additional work, Kim [27] indicated a tensile elongation to fracture in the 200–400 % range, as shown Fig. 2.63. Here, strain hardening may be observed in the curve. The deformation mechanism in his tests was grain-boundary sliding. To calculate the grain-size exponent, p, one can use Eq. (2.20), as follows:

Rewrite relation (2.20) as

$$\dot{\varepsilon} = \frac{A\sigma^n}{d^p}\exp\left(-\frac{Q}{RT}\right) \tag{2.20}$$

This relation is often expressed as:

$$\dot{\varepsilon} = K\left(\frac{b}{L}\right)^p \sigma^n \exp\left(-\frac{Q_c}{RT}\right) \tag{2.22}$$

Clearly, these relations are equivalent when $A \equiv Kb^p$. In Eq. (2.22), $L \equiv d$ and b is the Burgers vector. Expressing Eq. (2.22) on a logarithmic scale and taking the derivative for the constant strain rate and temperature, one obtains the grain size exponent:

$$p = n\frac{\partial \ln \sigma}{\partial \ln L}\bigg|_{\dot{\varepsilon},T} \tag{2.23}$$

The final grain size, evaluated from fracture test specimens, is related to the maximum flow stress of the tensile test. Table 2.5 lists the final grain sizes, the

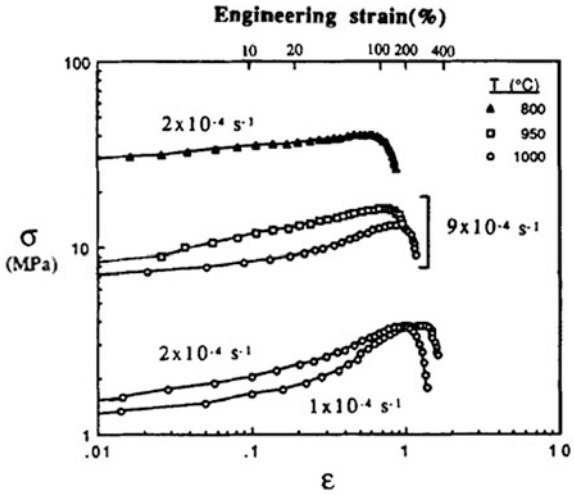

Fig. 2.63 True stress–true strain curves obtained by tension of extruded and pressed iron carbide at the temperatures indicated and at various constant true strain rates [27]. With kind permission from Springer Science+Business Media B.V.

Table 2.5 Values of grain size exponent, p for the extruded and pressed 5.25 % C carbide [27] (with kind permission from Springer Science+Business Media B.V.)

T (°C)	$\dot{\varepsilon}$ (s^{-1})	$L_{initial}$ (μm)	L_{final} (μm)	σ_{max} (MPa)	σ_{min} (MPa)	n	p
1000	1×10^{-4}	3.4	6.70	3.75	1.25	1.66	2.69
1000	2×10^{-4}	3.4	5.36	3.70	1.5	1.66	3.28
1000	9×10^{-4}	3.4	5.10	13.2	7.0	1.66	2.73
950	9×10^{-4}	3.4	4.94	16.0	8.7	1.66	2.71
800	2×10^{-4}	3.4	3.98	40.05	30.05	1.66	3.03
						Average	2.9

stress exponents, the grain-size exponents and other relevant parameters of this test.

In addition to the extruded and pressed carbides, also fabrication by HIP and pressure were performed. A comparison of the strain rate versus flow stress of these two kinds fabrication methods in carbides may be seen in Fig. 2.64 at three temperatures. Figure 2.65 shows the variations of strain rate versus flow stress on a logarithmic scale for extruded and pressed iron carbide at several temperatures. Depending on the temperatures, two values of the stress exponent were calculated from the slopes, as shown in Fig. 2.65: the value of 2 represents testing at the

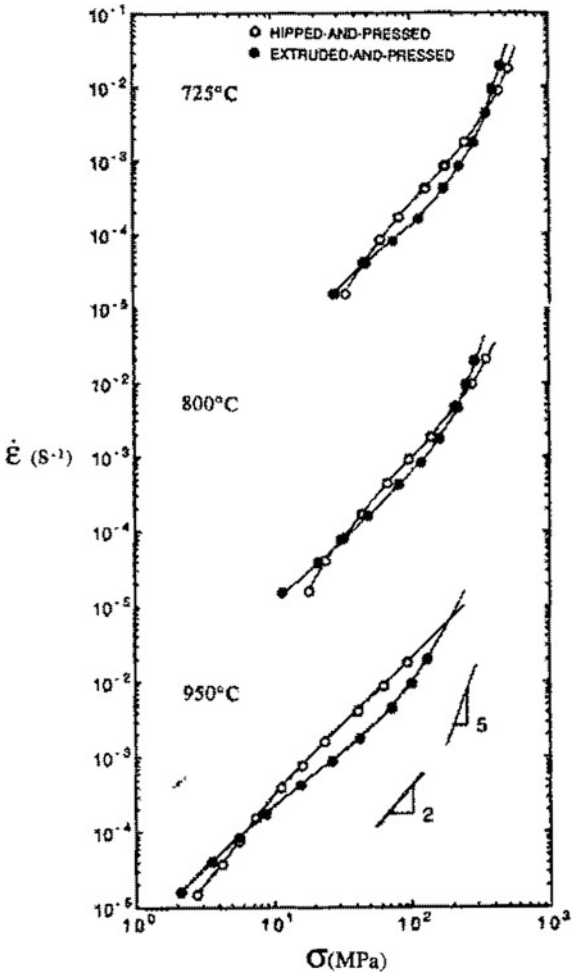

Fig. 2.64 Comparison of strain rate versus flow stress for the carbide fabricated by the methods indicated in the figure at three temperatures [27]. With kind permission from Springer Science+Business Media B.V.

725–1050 °C temperature range, whereas, above this temperature, the value is 1. The change in slope value is likely indicative of a different plastic flow mechanism. It is possible that at these low stresses and higher temperatures creep occurs.

The strain rate change with flow stress relation determined by tension is compared with the data obtained under compression, shown in Fig. 2.66 at two temperatures. Note the microstructure of the hipped and pressed iron carbide after large compressive deformation at 950 °C and at an initial strain rate of 6.67×10^{-3} s^{-1}, as shown in Fig. 2.67. Observe the grains that remain equiaxed after the deformation, suggesting that the deformation mechanism was, indeed, grain-boundary sliding. Also note that no cracks developed (see Fig. 2.67). The activation energy may be expressed either from Eq. (2.20) or (2.22). Consider

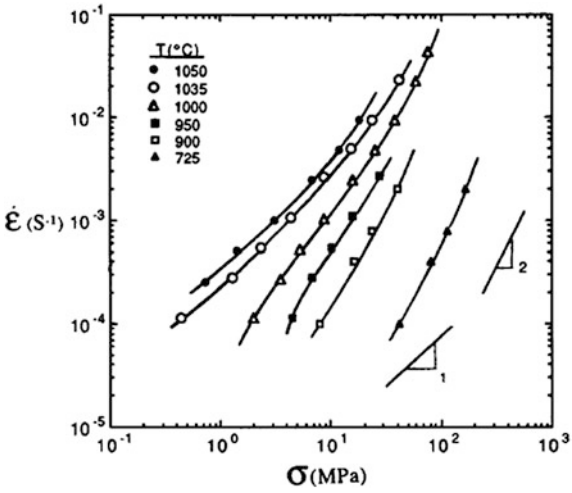

Fig. 2.65 Strain rate versus flow stress by tension test is indicated for iron carbide [27]. With kind permission from Springer Science+Business Media B.V.

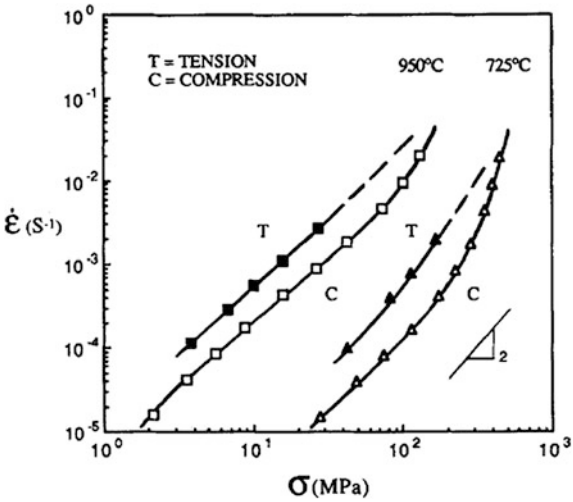

Fig. 2.66 Comparison of the tension and compression of the strain rate change versus flow stress at two temperatures [27]. With kind permission from Springer Science+Business Media B.V.

Eq. (2.22); express it on a logarithmic scale and take the derivative of strain rate with 1/T at constant stress and grain size to obtain the expression:

$$Q_c = -R \frac{\partial \ln \dot{\varepsilon}}{\partial 1/T}\bigg|_{\sigma,L} \tag{2.24}$$

A plot expressing this relation for deformation under tension and compression is shown in Fig. 2.68 for several stress exponents. The activation-energy values are indicated on the plot and they are in the range of 200–420 kJ/mol; the lower value is for n = 2 and the higher activation energy is for n = ∼1.

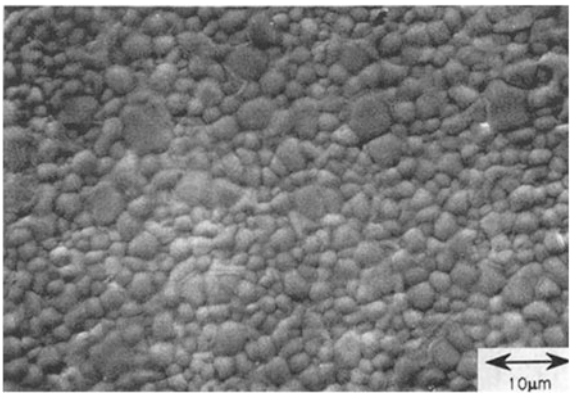

Fig. 2.67 Microstructure of the hipped and pressed iron carbide after large compressive deformation ($\varepsilon = -2.81$) [27]. With kind permission from Springer Science+Business Media B.V.

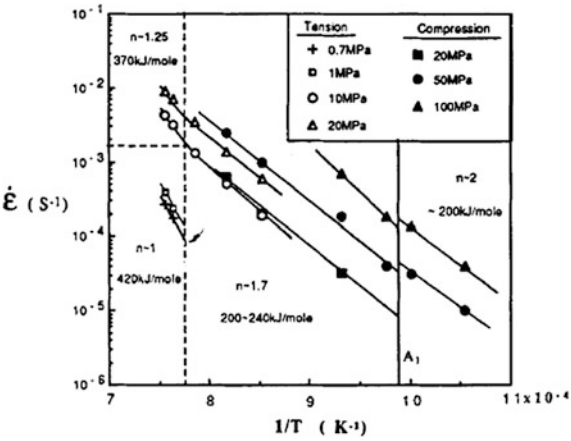

Fig. 2.68 Activation energies from tension and compression strain rate change [27]

2.2 Ductility in Single Crystal Ceramics

Figure 2.69 shows additional stress–strain curves of single crystals of MgO, deformed under compression in the [100] direction and temperature range of −196 to 1200 °C. In Fig. 2.33, the loading axis was ⟨111⟩ and in Fig. 2.36, the deformation was performed on a polycrystalline material. Note that the temperature range in Fig. 2.33 is 349–1204 °C, different than in Fig. 2.69. These crystals show considerable elongation at all temperatures and, at RT, they may be deformed plastically to about 6 %, as seen in Fig. 2.69a, before fracture sets in. This value of strain is considerably higher than the one obtained for polycrystalline MgO (as shown in Fig. 2.36), where only a strain of ∼0.0075 is indicated. Strain hardening is observed in these figures at all temperatures. It is known that the resistance of a material to deformation increases with the number of slip systems activated and the dislocation bands, which act as barriers to dislocation movement, generally occurring at slip-band intersections. Figure 2.70 shows the dislocation

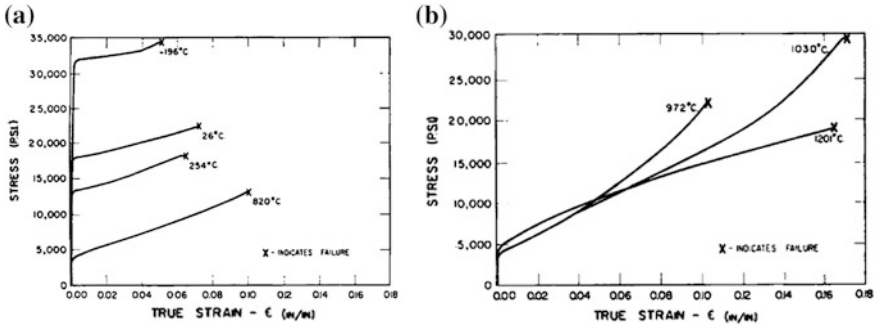

Fig. 2.69 Stress–strain curves of MgO single crystals deformed by compression in the [100] direction at various temperatures. **a** Temperature range −196 to 820 °C; **b** temperature range 972–1200 °C [2]. With kind permission of Wiley and Sons

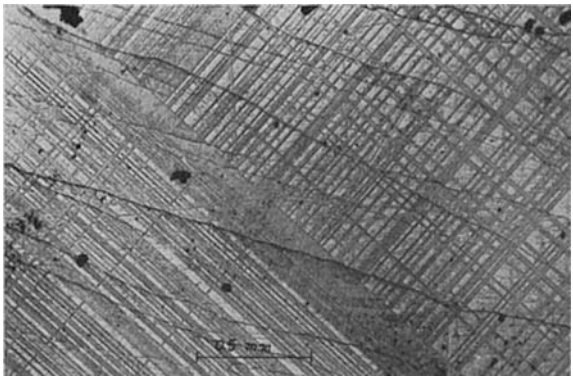

Fig. 2.70 Dislocation band structure. The single crystal was deformed in [100] direction [2]. With kind permission of Wiley and Sons

band structure deformed in the [100] direction. In this figure, the slip on one set of (110) planes encountered difficulty in passing through the slip bands formed on conjugate planes, a set of (110) planes. The thickness of the bands increases the resistance of the dislocations passing through them.

The stress–strain data were obtained at a constant rate of loading. The effect of the loading rate at three different rates is shown in Fig. 2.71. As may be seen from the curve, the slower loading rate resulted in (a) a lowering of the yield stress, (b) an increase in the plastic strain and (c) a decrease in the work-hardening rate. In other words, when testing these MgO crystals at a loading rate of 0.382 lbs/sq. in./s, the elongation was above 9 %.

Bear in mind that tests providing mechanical property data, such as ultimate strength, etc., may be considered extremely sensitive to the experimental conditions and the data are usually more scattered than those in similar tests of metallic materials.

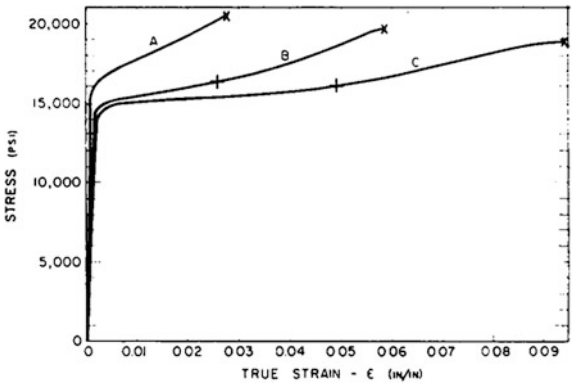

Fig. 2.71 Stress–strain curves of MgO obtained by compression in the [100] direction loaded at the strain rates of A 80.7, B 3.48 and C 0.382 lbs/sq. in./s. The + sign indicates the appearance of first visible crack [2]. With kind permission of Wiley and Sons

Another good example of single-crystal data regarding ductility or stress–strain relations is the case of zirconia (ZrO_2). ZrO_2 is considered to be a promising engineering material in comparison with other ceramics, because it reveals higher serviceability under different loading conditions, even up to 1400 °C.

Figure 2.72 presents an Y_2O_3-stabilized single crystal of ZrO_2 with other ceramics. Here, the crosshead speed, V_{ch}, is in the 0.005–5.0 mm/min range. These specimens were loaded in four-point bending under isothermal conditions. In this figure, the power parameter in the relation $V = M.K_I^N$ is on the ordinate N ($\equiv$ n in other terminology), where M is a parameter and K_I is the stress-intensity factor at the crack tip. Here, the deformation and strength of zirconia crystals at different temperatures and deformation rates are compared with the most widely used engineering ceramics, such as silicon nitride and alumina, under similar loading conditions. Thus, a general, comparative picture of the mechanical behavior of different types of ceramics and zirconia single crystals, over a wide range of temperatures and deformation rates, is obtained.

Compare the stress values and the deflection of the single-crystal zirconia (in particular, Y-PSZ-3) with those of the other ceramics presented. Table 2.6 shows some of the properties investigated, among them that of Y-PSZ-3. Note its ultimate strain reaching 44.0×10^{-4} m/m, obtained at a crosshead rate of $V_{ch} = 0.5$ mm/min. Furthermore, Table 2.7 may be also consulted for some of the properties of the various zirconia at 1400 °C. The deviation from linearity (elastic deformation) for zirconia was in the 1000–1100 °C range (not shown in Fig. 2.72). The strain at the elastic limit was in the range of $31.2–35.8 \times 10^{-4}$ m/m, depending on the rate of deformation (see Table 2.7). Also note that the ultimate strain of Y-PSZ-3 at an orientation of $\langle 111 \rangle$ is the highest of the various zirconia. In Fig. 2.73, the load versus the deflection is indicated for different strain rates and temperatures.

Load versus deflection diagrams for Y-FSZC-10 and Y-PSZC-3 are compared in Fig. 2.74.

Additional experiments on stress and strain, providing information on ductility, may be seen in Fig. 2.75. This figure illustrates the brittle and ductile failure modes and the strain-rate dependence of yield stress. These different failure

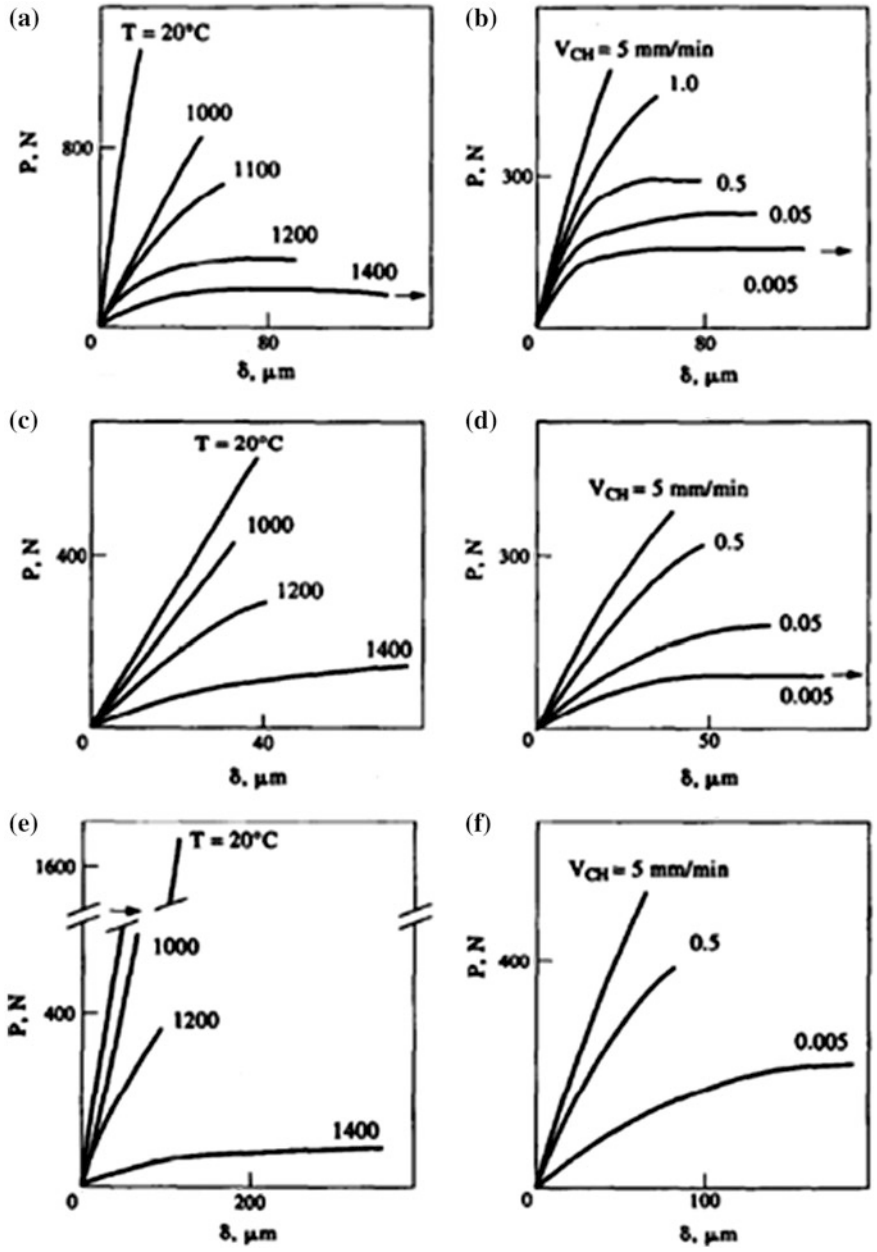

Fig. 2.72 The influence of the temperature, T (diagrams **a**, **c**, **e**) at $V_{ch} = 0.5$ mm/min and of the speed V_{ch}, (diagrams **b**, **d**, **f**) at $T = 1200$ °C on the appearance of the load (P) versus deflection δ: **a**, **b** SN-1; **c**, **d** A-l; **e**, **f** Y-PSZ-3. SN-1 is a silicon nitride-based ceramic with additions of Y_2O_3 and Al_2O_3; A-1 is an alumina-based ceramic with an addition of MgO; and Y-PSZ-3 is a Y_2O_3 stabilized zirconia based single crystal [18]. With kind permission of Elsevier

Table 2.6 Physico-mechanical characteristics of investigated ceramics and crystals at ambient temperature (average values) [18] (with kind permission of Elsevier)

Material (orientation of the specimen axis)	Density (g/cm^3)	Ultrasonic velocity (m/s)	Elastic modulus (GPa)		Bending strength (MOR)[a] (MPa)	Ultimate strain[a] ($\times 10^{-4}$ m/m)
			Dynamic	Static[a]		
Ceramics						
SN-1	3.21	9289	277	280	465	16.6
SN-2a	3.27	9690	307	305	510	16.7
A-1	3.70	9347	323	320	300	9.4
Y-PSZ-3	5.94	5951	210	207	908	44.0
Crystals						
Y-FSZC-10 (⟨101⟩)	5.87	5933	207	180	134	7.4
Y-FSZC-20 (⟨101⟩)	5.76	6116	215	185	140	7.6
Y-PSZC-3 (⟨111⟩)	6.04	5394	176	149	642	43.0

Table 2.7 Average values of mechanical characteristics of investigated crystals at 1400 °C [18] (with kind permission of Elsevier)

Material	V_{ch} (mm/min)	Elastic limit (MPa)	Upper yield point[a] (MPa)	Lower yield point (MPa)	Strain at elastic limit ($\times 10^{-4}$ m/m)	Strain[a] at upper yield point (MPa)	Elastic modulus (GPa)
Y-FSZC-10	5.0	274	–	–	17.5	–	157
	0.5	327	445	445	23.2	51.5	141
	0.05	269	338	318	18.7	32.2	144
	0.005	210	250	234	16.9	28.4	124
Y-FSZC-20	5.0	213	–	–	–15.3	–	140
	0.5	300	–	–	21.6	–	139
	0.005	276	324	295	23.2	35.7	119
Y-PSZC-3	5.0	393	444	–	31.2	37.5	126
	0.5	403	475	–	33.0	42.5	122
	0.05	400	550	–	32.8	75.2	122
	0.005	390	556	–	35.8	74.4	109

[a] For Y-PSZC-3 crystals—ultimate stress and strain values

modes, which relate to the presence or absence of plastic deformation, presumably result from the various orientations of the easy slip planes in the specimens, relative to the applied stress. Notice the inset indicating a 7.8 % permanent strain. In Fig. 2.76, strength is plotted versus test temperature for partially-stabilized zirconia (henceforth: PSZ), cubic ZrO_2 crystals, polycrystalline PSZ and hot-pressed Si_3N_4. At 1500 °C, the cubic ZrO_2 specimens either failed in a brittle manner or exhibited significant plasticity, depending on their crystallographic orientation. The strengths of those cubic ZrO_2 specimens exhibiting plasticity depended significantly on strain rate, with their flexural strengths decreasing with decreasing strain rate.

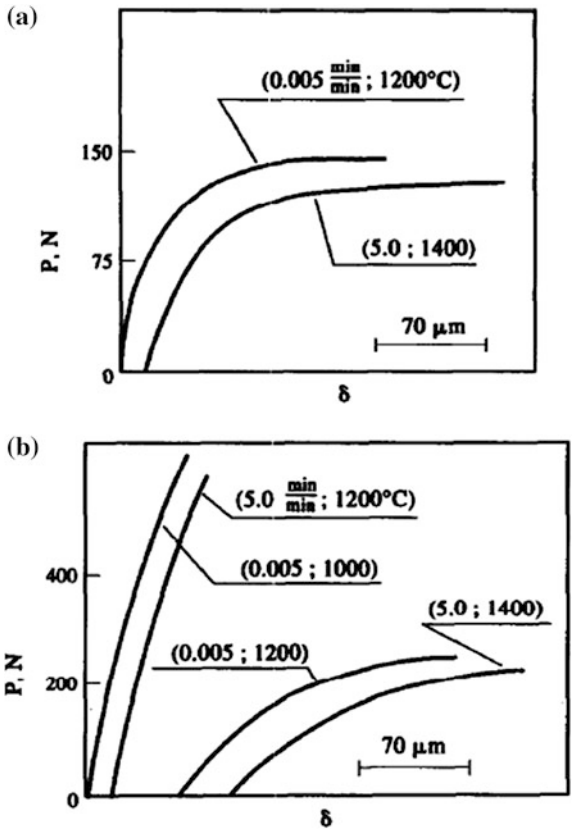

Fig. 2.73 Load versus deflection diagrams for **a** SN-1 and **b** Y-PSZ-3 under different conditions of deformation [18]. With kind permission of Elsevier

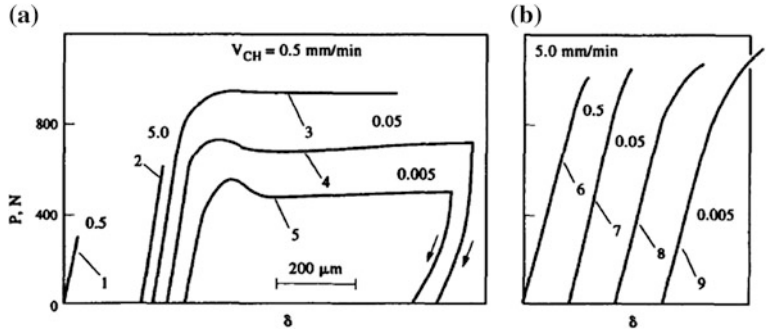

Fig. 2.74 Load versus deflection diagrams for **a** Y-FSZC-10 and **b** Y-PSZC-3 at various V_{ch} and **T** = 20 °C (1) and 1400 °C (2–9). *Arrows* show specimen unloading [18]. With kind permission of Elsevier

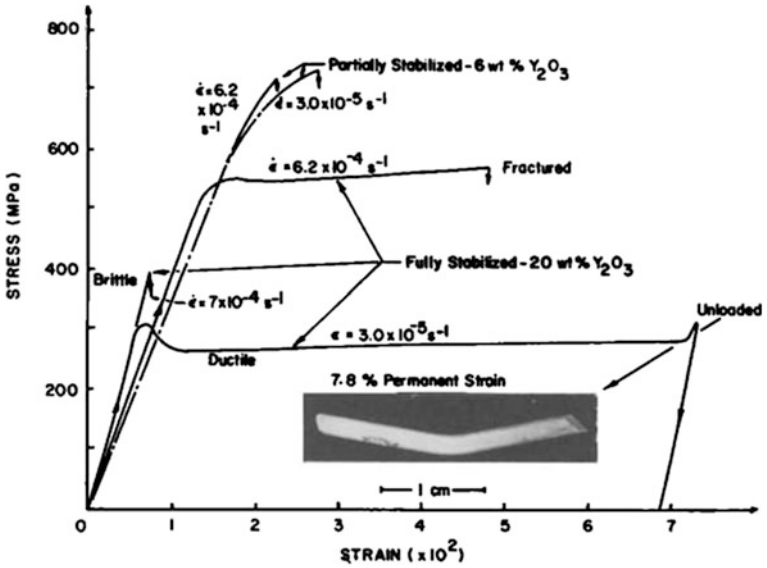

Fig. 2.75 Stress–strain behavior at 1500 °C of partially and fully stabilized zirconia single crystals vis. strain rate. Inset shows permanent deformation achieved in fully stabilized specimen [24]. With kind permission of Wiley and Sons

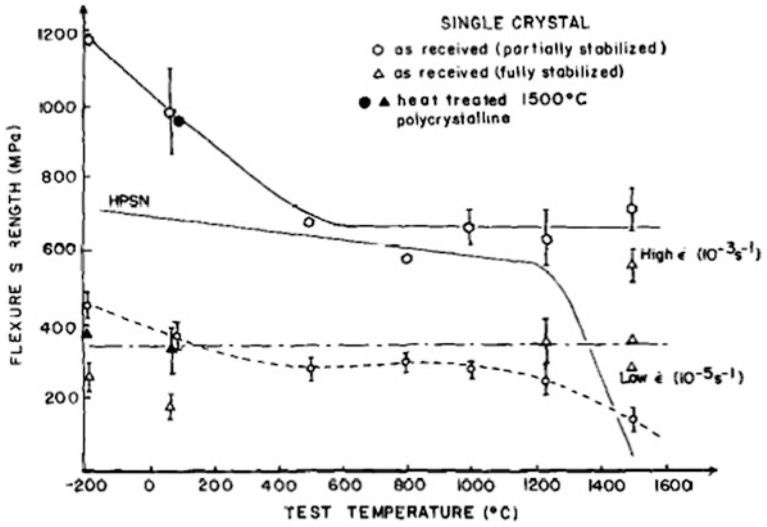

Fig. 2.76 Temperature dependence of flexural strength of partially and fully stabilized zirconia single crystals, polycrystalline PSZ, and hot-pressed Si_3N_4 (HPSN). PSZ is partially stabilized ZrO_2 with Y_2O_3 [24]. With kind permission of Wiley and Sons

The results for strength and toughness of PSZ single crystals indicate a significant potential for the development of high-strength, high-temperature structural ceramics, in which excellent retention of mechanical properties up to ~ 1500 °C is achieved. Thus, in contrast to many ceramics, the strength of zirconia crystals remains practically unchanged in partially-stabilized crystals and even increases in fully-stabilized ones.

2.3 Summary

The challenge of ceramists and materials scientists is to make ceramics ductile at RT and low temperatures, in order to extend the use of ceramic materials to more applications. This is not a trivial goal, since the nature of ionic and covalent bonding must be overcome by introducing dislocations and making their mobility possible. Dislocations are primarily responsible for plastic deformation. In the last decade, much effort has been made to develop ductile materials exhibiting proper slip planes that enable dislocation movement. Dislocations are present in ceramics and their role, in most ceramics, is best observed at high temperatures. However, at low and moderate temperatures, their motion is limited, since the stress required for their movement is high, usually above their fracture stress, so that fracture sets in before yielding. Different mechanisms may be responsible for the BDT, such as: grain size, an additional second phase, structural modification (preferably to nanostructure), etc. Single crystals are likely to be the best candidates for the development of appreciable ductility, since they have no inherent grain boundaries (or sliding) to interfere with dislocation motion.

References

1. Dieter GE (1986) Mechanical metallurgy, 2nd edn. McGraw-Hill Inc., New York
2. Hulse CO, Pask JA (2006) J Am Ceramic Soc 43, 373
3. Jillavenkatesa A, Dapkunas SJ, Lum, L-SH (2001) Special publication 960-1, Particle size characterization
4. Nagano T, Kaneko K, Zhan G-D, Mitomo M, Kim Y-W (2002) J Eur Ceram Soc 22:263
5. Nanjangud SC, Brezny R, Green DJ (1995) J Am Ceram Soc 78:266
6. Parker ER, Pask JA Washburn J (1962) Ductile ceramics research, California University, Berkley Institute of Engineering Research, Defense Technical Information Center
7. Pelleg J (2013) Mechanical properties of materials. Springer, Dordrecht
8. Prochazka S (1975) The role of boron and carbon in the sintering of silicon carbide. In: Popper P (ed.) Special ceramics, 6th edn. British Ceramic Research Association, Stoke-on-Trent, p 171
9. Rothman A, Kalabukhov S, Sverdlov N, Dariel MP, Frage N (2012) Int. J Appl Ceram Technol 1:11
10. Trunec M (2008) Ceramics—Silikáty 52:165

Further References

11. Anstis GR, Chantikul P, Lawn BR, Marshall DB (1981) J Am Ceram Soc 64:533
12. Basu B, Venkateswaran T, Kim D-Y (2006) J Am Ceram Soc 89:2405
13. Brunner D, Baghbadrani ST, Sigle W, Rühle M (2001) J Am Ceram Soc 84:1161
14. Castaing J, Cadoz J, Kirby SH (1981) J Phys (Paris), Colloq C3 42:43–47
15. Chen Y-f., Xiao S-l, Tian J, Xu L-j, Chen Y-y (2011) Trans Nonferrous Met Soc China 21:342
16. Fahrenholtz WG, Hilmas GE, Talmy IG, James A, Zaykoski J (2007) Am Ceram Soc 90:1347
17. Gogotsi GA (2003) Ceram Int 29:777
18. Gogotsi GA, Ostrovoy DY (1995) J Eur Cer Soc 15:271. (With kind permission of Elsevier)
19. Gong J, Wang J, Guan Z (2002) J Mater Sci 32:865
20. Gorun AE, Parker ER, Pask JA (1958) J Am Ceram Soc 41:151
21. Grady DE, Lipkin J (1980) Geophys Res Lett 7:255
22. Hall EO (1951) Proc Phys Soc London 643:747
23. Hulse CO, Copley SM, Pask JA (1963) J Am Ceram Soc 46:317
24. Ingel RP, Lewis D, Bender BA, Rice RW (1982) Commun Am Ceram Soc C-150:65
25. Ishihara S, Bill J, Aldinger F, Wakai F (2003) Mater Trans 44:794
26. Kim H-S, Roberts S (1994) J Am Ceram Soc 77:3099
27. Kim W-J, Wolfenstine J, Ruano OA, Frommeyer G, Sherby O (1992) Met Trans A 23A:527
28. Kim W-J, Wolfenstine J, Sherby O (1991) Acta Metal Mater 39:199
29. Kingery WD, Pappis J (1956) J Am Ceram Soc 39:64
30. Lam DCC, Lange FF, Evans AG (1994) J Am Ceram Soc 77:2113
31. Langdon TG (1994) Acta Metall At Mater 42:2437
32. Lankford T (1996) J Mater Sci Letters 15:745
33. Lankford T Jr (1995) Office of naval research, Arlington, VA 22217, prepared by Southwest Research Institute, San Antonio
34. Li W, Zhang X, Hong C, Han W, Han J (2009) J Eur Ceram Soc 29:779
35. Mangalaraja RV, Chandrasekhar BK, Manohar P (2003) J Mater Sci Eng A343:71
36. Miyoshi T, Funakubo H (2010) Jpn J Appl Phys 49, 09MD13
37. Palmqvist S (1962) Arch Eisenhuettenwes 33:629
38. Parker ER, Pask JA, Washburn J, Gorum AE, Luhman W (1958) J Metals 10:351
39. Petch NJ (1953) J Iron Steel Inst London 173:25
40. Shinoda Y, Nagano T, Gu H (1999) J Am Ceram Soc 82:2916
41. Srinivasan M, Stoebe TG (1970) J Appl Phys 41:3726
42. Stokes RJ, Johnston TL, Li CH (1959) Trans AIME 215:43744
43. Stokes RJ, Li CH (1963) J Am Ceram Soc 46:423
44. Suzuki H (1983) Ceramics 3
45. Taylor GI (1938) Plastic strain in metals. J Inst Metals 62:307
46. Tsukuma K, Vasahiko (1985) J Mat Sci 20:1178
47. Wakai F, Kondo N, Shinoda Y (1999) Curr Opin Solid State Mater Sci 4:461
48. Wakai F, Sakaguchi S, Matsuno Y (1986) Adv Ceram Mater 1:259
49. Wang C-M, Mitomo M, Emoto H (1997) J Mater Res 12:3266
50. Yan W, Li N, Li Y, Liu G, Han B, Xu J (2011) Bull Mater Sci 34(5):1109 (Indian Academy of Sciences)
51. Zhan G-D, Mitomo M, Nishimura T, Xie R-J, Sakuma T, Ikuhara Y (2000) J Am Ceram Soc 83:841

http://www.springer.com/978-3-319-04491-0

Mechanical Properties of Ceramics

Pelleg, J.
2014, XXII, 765 p. 780 illus., 169 illus. in color.,
Hardcover
ISBN: 978-3-319-04491-0